Materials Advances

ROYAL SOCIETY OF CHEMISTRY

REVIEW

View Article Online
View Journal | View Issue



Cite this: *Mater. Adv.*, 2022, 3, 6096

# Implementation of heteroatom-doped nanomaterial/core–shell nanostructure based electrocatalysts for fuel cells and metal-ion/air/sulfur batteries

Saravanan Nagappan,*[a] Malarkodi Duraivel,[b] NaHyun Park,[a] Kandasamy Prabakar [b] and Kang Hyun Park *[a]

Core–shell nanostructures (CSNs) have been extensively used in energy conversion and storage (ECS) applications. CSNs feature abundant active sites and large surface areas. In addition, their size, shape, and morphology can be tailored to be uniform and controlled. The catalytic activity and performance of CSNs can be significantly improved by heteroatom doping to CSNs, which makes them even more advantageous for ECS applications. In addition to various noble metals, transition metals have been used in the cores and shells of nanostructures featuring heteroatoms. Such materials are inexpensive and exhibit excellent catalytic activity and stability. Likewise, heteroatom-doped nanomaterial and core–shell nanostructure (HCSN) based electrocatalysts serve as bifunctional electrocatalysts for the oxygen reduction reaction (ORR) and hydrogen evolution reaction (HER) as well as the ORR and oxygen evolution reaction (OER). These bifunctional electrodes are highly suitable for fuel cell and battery applications. In this review article, we exclusively focus on the important role of HCSNs in various types of fuel cells and batteries. In particular, we discuss the important roles and applications of HCSNs in proton exchange membranes (PEMs), anion exchange membranes (AEMs), direct methanol, microbial, and other types of fuel cells as well as metal ion batteries such as lithium (Li), sodium (Na), and potassium (K)-ion batteries. The applications of HCSNs in Li–sulfur (S) batteries and metal–air batteries, such as Li, zinc (Zn), and Na–air batteries, have also been addressed. Finally, we have discussed the technical advancements related to the applications of HCSNs in fuel cells and batteries along with their disadvantages, scope, and future prospects. This review will benefit researchers working in the ECS field as well as those investigating various other applications, such as drug delivery, sensors, and adsorption.

Received 7th April 2022,
Accepted 29th June 2022

DOI: 10.1039/d2ma00390b

rsc.li/materials-advances

[a] *Department of Chemistry, Chemistry Institute for Functional Materials, Pusan National University, Busan, 46241, Republic of Korea. E-mail: chemistry@pusan.ac.kr, saravananagappan@gmail.com*

[b] *Department of Electrical Engineering, Pusan National University, 2 Busandaehak-ro 63beon-gil, Geumjeong-Gu, Busan 46241, Republic of Korea*

**Saravanan Nagappan**

*Saravanan Nagappan is working as a Post-Doc Fellow under Professor Kang-Hyun Park in the Department of Chemistry and Chemistry Institute for Functional Materials, Pusan National University, Korea. His research interests include the synthesis and fabrication of various organic–inorganic hybrid nanomaterials, MXenes, graphene, carbon, and nanoclay based materials for coatings, catalysis, environmental remediation, biomedicine, electrocatalysis, and energy storage and conversion applications.*

**Malarkodi Duraivel**

*Malarkodi Duraivel will obtain her PhD, in Electrical and Electronics Engineering (August 2022) under the supervision of Professor Kandasamy Prabakar at Pusan National University, Korea. Her current research focuses on the development of low-cost and efficient electrocatalysts for energy conversion applications including water splitting and oxygen reduction reactions.*

## 1. Introduction

Research on core–shell nanostructures (CSNs) has attracted considerable interest due to the continuous demand for electrocatalysts with improved performance and stability that are suitable for energy conversion and storage (ECS) applications.[1–5] Various transition metals, metal oxides, and noble metals are used to construct the cores and shells of CSNs which are used in drug delivery, energy and environmental applications, and catalysis, among others.[6–11] Numerous methods have been employed to synthesize CSNs based on top-down and bottom-up approaches.[12] Micro-fabrication methods or various electrical, mechanical, and optical tools (*e.g.*, lithographic, laser treatment, mechanical mixing, and polishing techniques) are used to develop CSNs *via* top-down approaches.[12] In contrast, bottom-up approaches involve the alteration of the chemical properties using self-assembly and seed-growth techniques, sol–gel processes involving the Stöber method, film deposition and growth, colloidal aggregation, and chemical vapor deposition (CVD), among others.[12] These methods have unique advantages and disadvantages based on surface finishing and metal compositions. Compared to top-down approaches, bottom-up approaches are simpler, cost-effective, and considerably easier to reproduce without using expensive instrumental set-ups. They also ensure control of the nanoparticle size, structure, and morphology. Top-down and bottom-up approaches can be combined by first constructing a uniform core *via* a top-down approach, followed by a thin shell layer by a bottom-up approach to afford significantly improved and controlled nanoarchitectures, which are extremely useful for electrocatalytic applications.[12]

Platinum (Pt), palladium (Pd), iridium (Ir), ruthenium (Ru), rhodium (Rh), gold (Au), and other expensive noble metals were widely used in ECS owing to their superior electrochemical properties and stability compared to transition metals.[7,13,14] The high cost and insufficient availability of Pt and other noble metals limit their use in practical and commercial applications, such as fuel cells and batteries. Several attempts have been made to minimize noble metal consumption by alloying them with inexpensive and earth-abundant transition metals (M = cobalt (Co), nickel (Ni), manganese (Mn), iron (Fe), aluminum (Al), magnesium (Mg), and tin (Sn), among others).[13–20] Among various structurally and morphologically distinct nanomaterials, CSNs have been widely used in ECS applications due to their advanced properties and precisely controlled morphologies and chemical compositions (core or shell). In addition, their core and shell structures can be conveniently controlled using single or multiple layers.[4,6] Long *et al.* studied the effective role of Pt and Pt–Pd core–shell nanoparticles in electrocatalysts.[16] Pt–Pd core–shell nanoparticles were synthesized by a modified polyol method using silver nitrate ($AgNO_3$) as a support in the presence of ethylene glycol.[16] Jian *et al.* developed efficient CSNs (CNT@$RuO_2$) *via* the sol–gel method using carbon nanotubes (CNTs) and ruthenium oxide ($RuO_2$).[21] These CSNs served as bifunctional catalysts, with superior performances in both the oxygen reduction reaction (ORR) and oxygen evolution reaction (OER), and also delivered appreciable results in rechargeable Li–air batteries. The CNT core (15 nm in diameter) and $RuO_2$ shell (thickness of approximately 3.5 nm) demonstrated outstanding catalytic activity and usability in Li–air batteries.[21] The Li–air battery cell fabricated using the CNT@$RuO_2$ nanocomposite exhibits a high round-trip efficiency (*ca.* 79%) at a

**NaHyun Park**

*NaHyun Park is currently pursuing a Master's in the Department of Chemistry at Pusan National University, Korea. Her research interests focus on the development of nanomaterials for battery applications.*

**Kandasamy Prabakar**

*Kandasamy Prabakar is a Professor at the Department of Electrical Engineering, Pusan National University, Korea. His current research is focussed on the development of various nanohybrid electrodes for energy conversion and storage applications. In particular, he is working on the development of novel electrodes for hybrid capacitors, photo-electrocatalytic hydrogen and oxygen evolution reactions for total water-splitting, and reduction reactions for metal–air batteries.*

**Kang Hyun Park**

*Kang Hyun Park is a Professor at the Department of Chemistry and Chemistry Institute for Functional Materials, Pusan National University, Korea. His research interests include the development of new transition metal-nanoparticle catalyzed reactions. Currently, his research is focused on the development of multifunctional nanohybrid materials for electrocatalysis, especially on the synthesis of multifunctional nanohybrid electrodes for fuel cell and battery applications.*

current of 100 mA $g_{total}^{-1}$ with superior cycling stability and high rate performance.[21]

Heteroatom doped nanomaterials and core–shell nanostructures (HCSNs) are highly decorated with heteroatoms on the surface or in the chemical structures, and the presence of low-cost and earth-abundant metals either in the core or in the shell or noble metal deposits (a few layers thick) on the shells can enhance their electrocatalytic properties, stability, and tolerance against severe environmental conditions.[22,23] Single heteroatoms, such as N, S, P, and boron (B), or combinations of two or more such heteroatoms are suitable for various applications due to the enhanced electrochemical activity which results from the formation of oxygen vacancies and defects in metal-based catalysts.[24,25] Furthermore, doping heteroatoms with earth-abundant transition metals or conjugated polymers leads to improved properties and stability concerning different electrochemical applications.[26,27] Heteroatom doping on CSNs has many unique advantages. It increases the number of active sites on the CSN surface, enhances the electrochemical activity and conductivity, facilitates charge transfer from the CSNs and heteroatoms, and improves the stability of the catalysts.[28] The particle size, shape, morphology, and chemical compositions of the core and shell are amenable to precise control, which facilitates the development of CSNs and HCSNs tailored for various ECS applications. Despite the difficulties related to dissolution under acidic conditions, these nanostructures offer the major advantages of high surface area and pore volume, more active sites and defects, and reduced use of noble metals. The disadvantages can be overcome through the appropriate selection of materials to maximize production and minimize the cost of the electrocatalysts. Typically, heteroatom doping is performed either using a direct *in situ* doping technique, such as CVD, bottom-up synthesis, and ball-milling, or post-synthetic treatments, such as wet chemical methods and thermal annealing.[28] The valence electron numbers and sizes of N and B are almost identical to those of carbon (C). Therefore, it is easier to dope graphene-based C materials with N and B than with other heteroatoms.[28] Various N-, B-, S-, and P-based compounds have been used for heteroatom doping on CSNs using different *in situ* doping techniques or post-synthetic treatments.[12,28,29] HCSNs feature highly oriented structures with large surface areas, porosity, and large numbers of active sites as well as defects. Recent attempts have focused on studying the role and theoretical background of multi-heteroatoms in electrocatalysis, particularly for the ORR owing to the increasing demand for highly stable ORR electrodes for numerous end-use applications.[23,24,30] In addition, continuous attention has been given to the use of HCSNs for various fuel cells and battery applications.[31–34]

The various aspects of CSNs related to ECS applications have been discussed in a few reviews.[4,35,36] Feng *et al.* briefly reviewed the important aspects and applications of CSNs with concern for storage systems including various types of supercapacitors and Li-based batteries, energy conversion systems, such as solar cells and fuel cells, and photocatalytic hydrogen production.[35] CSNs synthesized using transition metals and encapsulated in C materials were discussed thoroughly and the key advantages of CSNs for electrochemical applications were summarized.[36] The use of C-based CSNs is prevalent in various ECS applications due to their enhanced conductivity and catalytic activity compared to other materials.[4] Combinations of the various properties of the mentioned earth-abundant transition metals and C structures with those of the heteroatoms significantly improve the catalytic properties of CSNs.

Bai *et al.* synthesized N and S co-doped mesoporous C, followed by the deposition of manganese oxide ($MnO_2$) nanoflakes *via* a solvothermal reaction to obtain an excellent supercapacitor behavior of CSNs with a maximum capacitance of 310 F $g^{-1}$, energy and power densities of 44 W h $kg^{-1}$ and 12 000 W h $kg^{-1}$, respectively, and a 90% retention of capacitance after 5000 cycles.[37] Zhao *et al.* developed bifunctional heteroatom doped core–shell C fibers by first preparing composite nanofibers by an electrospinning technique using a mixture of polyacrylonitrile (PAN, $M_w$ = 230 000), polyvinylpyrrolidone (PVP, $M_w$ = 1300 000), and cobalt acetylacetonate ($Co(acac)_2$), dissolved in *N*,*N*-dimethylformamide (DMF).[38] The composite nanofibers were reacted with cobalt nitrate hexahydrate ($Co(NO_3)_2{\cdot}6H_2O$) and zinc nitrate hexahydrate ($Zn(NO_3)_2{\cdot}6H_2O$) in the presence of 2-methylimidazole (2-MeIM) *via* immersion in methanol to form metal–organic framework (MOF) based zeolitic imidazolate frameworks (ZIFs). The PAN@ZIFs were subjected to pyrolysis at 800 °C (at a heating rate of 2 °C $min^{-1}$) for 2 h in an $N_2$ atmosphere to obtain heteroatom doped core–shell C fibers. The as-prepared catalyst delivered excellent bifunctional catalytic activity for both the ORR and OER. The catalyst also functions as a primary rechargeable Zn–air battery with power and energy densities of 140.1 mW $cm^{-2}$ and 878.9 W h $kg_{zn}^{-1}$, respectively, and excellent long-term cycling stability (constant voltage gap after 150 h).[38]

Fig. 1 clearly illustrates the continuous growth of CSNs, heteroatom doping, and the utility of CSNs in fuel cells and battery applications. Recently, there has been an increase in the demand for CSNs for ECS applications due to their advanced properties and highly controlled size and morphology. Heteroatom doping of CSNs has been utilized for developing improved electrocatalysts for wider applications. We briefly reviewed the various aspects of synthesis and application of HCSN based electrocatalysts for the ORR,[1] whereas a few other review articles have focused on the role of heteroatom-doping of CSNs in ECS-related applications. However, none of them has discussed the relationship between the structural properties of HCSNs and their utility in various types of fuel cells and batteries. Their pertinence to future ECS demands has also not been commented on. Therefore, in this review, we exclusively cover the recent advances in HCSNs and their emerging applications in different fuel cells and batteries. A special emphasis has been placed on the role of HCSNs in ECS applications and suggestions have been provided for improving the properties and mitigating the disadvantages of HCSNs. This review is expected to provide constructive guidance to those working in related fields. Fig. 2 also illustrates the effective approaches of using heteroatom doped nanomaterials and core–shell

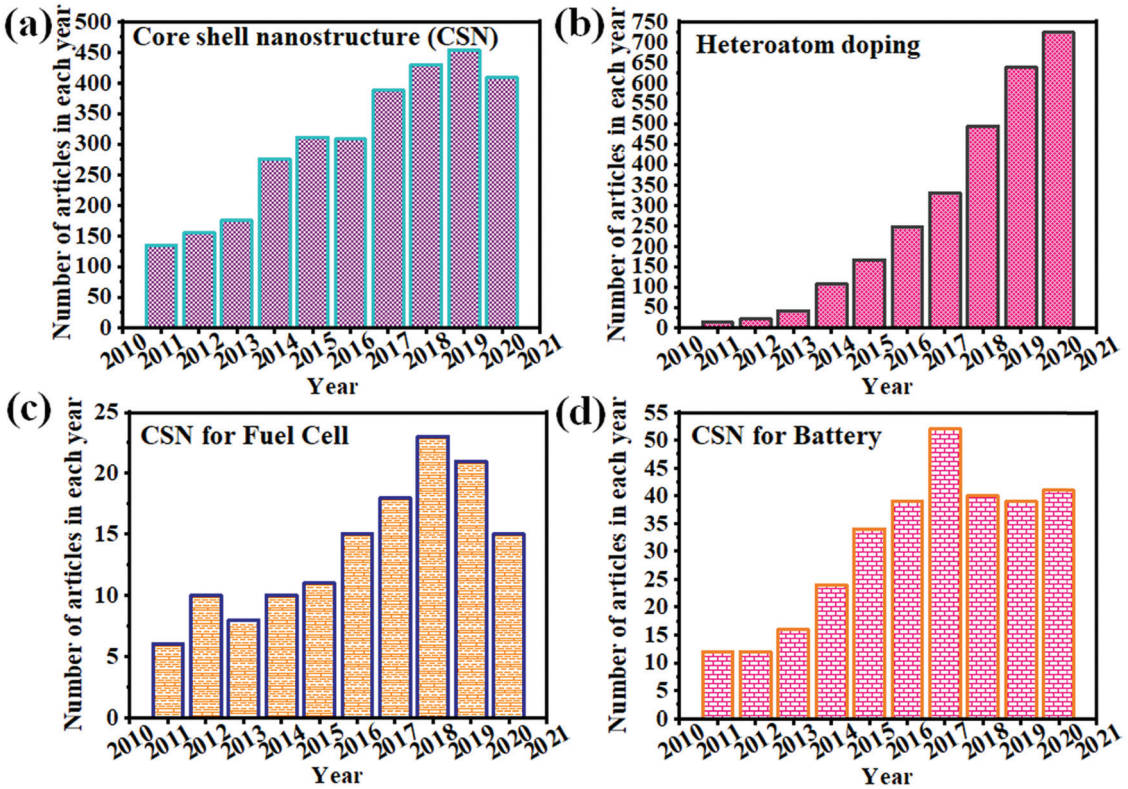


Fig. 1 Number of papers published under the topic of (a) core–shell nanostructures, (b) heteroatom doping, (c) CSNs for fuel cells, and (d) CSNs for batteries from 2011 to 2020 (source: https://apps.webofknowledge.com/).

nanostructures for various fuel cells and batteries. These approaches summarize that HCSNs play an effective role in various electrochemical ECS applications.

## 2. Implementation of heteroatom doped nanomaterials/core–shell nanostructures (HCSNs)

CSNs and HCSNs have considerable utility in biomedical, energy, and environmental applications. They are also used in catalysis, water treatment, and sensing applications.[12,24] Recently, CSNs and HCSNs have been used in ECS applications because of their improved properties, minimal use of noble metals, and reduced cost. The important applications of HCSNs in PEM, AEM, direct methanol, microbial, and other types of fuel cells have been discussed. In addition, HCSN applications in metal-ion batteries, such as Li-ion and Na-ion batteries, metal–air batteries, such as Li, Zn, and Na–air batteries, and metal–S batteries (MSBs) have also been addressed.

### 2.1. HCSNs for fuel cells

The combustion of fossil fuels produces electrical and thermal energies that are required for ECS applications.[39] However, the high consumption of fossil fuel generates various environmental

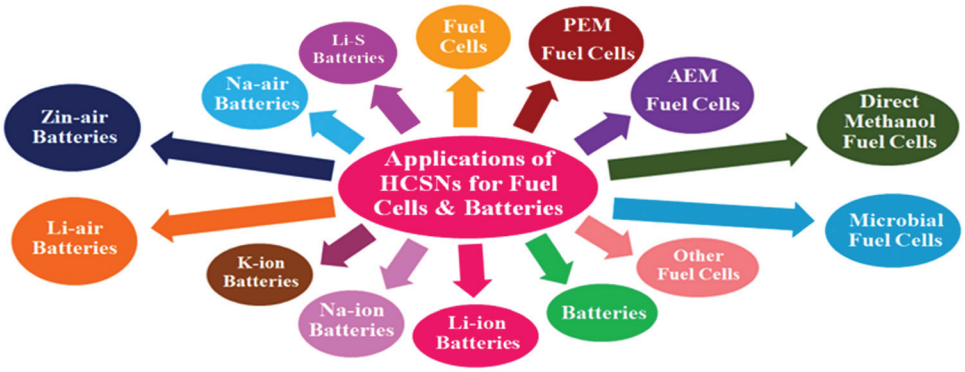


Fig. 2 The schematic illustration and applications of heteroatom doped nanomaterials and core–shell nanostructures for various fuel cells and batteries.

issues that can be mitigated by using alternative sources of electricity. Fuel cells are electrochemical devices that generate electricity by converting chemical energy to electrical energy.[40] A typical fuel cell consists of an anode, a cathode, and an electrolyte membrane.[41,42] Hydrogen is passed through the anode and oxygen is evolved at the anode of a fuel cell. At the anode side, hydrogen molecules are split into electrons and protons in the presence of a catalyst and transferred to the PEM. Electrons are simultaneously transferred to the circuit and produce electric current and heat. The protons, electrons, and oxygen combine at the cathode site to generate water.[41] Fuel cells are used widely to supply electricity to hospitals, homes, grocery stores, and business offices. They also provide energy to buses, trucks, cars, trains, and other vehicles.[41] Fuel cells are low-maintenance devices capable of continuous electricity generation.[41] Noble metals have been extensively used for high-performance fuel cell applications because they impart improved stability and longer working cycles compared to other materials.[43–45] On the other hand, noble metal catalysts are expensive and have poor tolerance to alcohol. Functional nanomaterials with enhanced properties have thus been developed as a viable replacement for noble metals. Various types of fuel cells fabricated using HCSN electrocatalysts have been discussed in the following sub-sections.

**2.1.1. HCSNs for proton exchange membrane fuel cells (PEMFCs).** PEMFCs mainly consist of a thin porous cathode and anode and a conductive electrolyte membrane, which typically features a perfluorinated polymer backbone with sulfonic acid side chains.[46] The polymer membrane is highly conductive under humidified conditions. In addition to the cathode, anode, and electrolyte membrane, the PEMFC assembly consists of a gas diffusion layer (GDL) which is mainly responsible for controlling the oxygen and hydrogen gas transfer through the cathode and anode layers.[46] Oxygen is reduced at the cathode and hydrogen is oxidized at the anode. Protons migrate from the anode to the cathode *via* the electrolyte membrane and electrons are carried over an external circuit load (Fig. 3). Oxygen reacts with protons and electrons at the cathode to produce heat and generate water as a by-product. PEMFCs are advantageous because they have high energy densities and specific power per unit volume and weight, and are capable of delivering a continuous supply of electrical energy. In addition, they have compact designs and quick start-up times and require minimum maintenance.[47] However, some of the disadvantages of PEMFCs are that they are expensive, have low tolerance against alcohol, and are susceptible to catalyst poisoning. Additionally, they exhibit sluggish kinetics at the cathode and exhibit difficulties in oxygen activation and O–O cleavage.[48] Electrocatalysts with superior ORR activities compared to commercial Pt/C catalysts have been used in PEMFCs or other fuel cell applications.[49,50] The cost of catalyst layers in PEMFCs, based on strategic analysis reports, was found to be approximately US \$11.24 $kW^{-1}$, of which US \$10 $kW^{-1}$ was used for Pt dosage.[48] Continuous efforts have been made to reduce the Pt loading of PEMFCs by employing various transition metals, metal oxides, carbon, and heteroatoms, to construct either the core or the shell.[48,51,52] Some advancements were made in PEMFC technology by Jiao *et al.* to meet the future energy demands.[53]

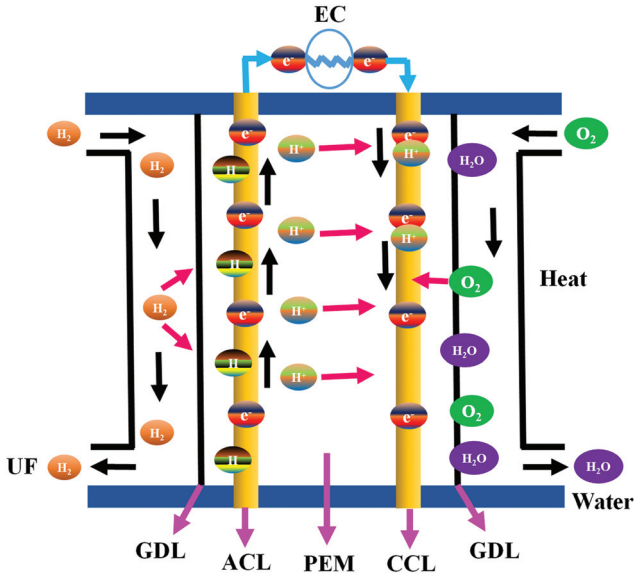


Fig. 3 The working principle of PEMFCs (note: $H_2$ – hydrogen, $O_2$ – oxygen, $H_2O$ – water, UF – unused fuel, GDL – gas diffusion layer, ACL – anode catalyst layer, PEM – proton exchange membrane, CCL – cathode catalyst layer, $H^+$ – proton, $e^-$ – electron).

The membrane electrode assembly (MEA), active electrode materials, water generation, and thermal management were improved compared with existing PEMFC set-ups.[53] Hydrogen and air (or oxygen) were passed through the anode and cathode sites during the PEMFC operation.[53] The hydrogen molecules dissociated into electrons and protons at the anode catalyst layer through the hydrogen oxidation reaction (HOR). The generated electrons passed through the external circuit, whereas the protons were exchanged through the PEM and migrated to the cathode catalyst layer. On the other hand, the diffused oxygen came in contact with the cathode conductive layer (to which the protons adhered) *via* the GDL and underwent the ORR, generating water, heat, and electricity.[53]

Recently, Jiang *et al.* briefly reviewed the role of electrocatalysts used to develop CSNs for the ORR. In particular, the authors discussed the important aspects of the obtained ORR electrocatalyst related to PEMFCs along with the approaches currently adopted to enhance the activity of CSN based electrocatalysts used in PEMFCs.[54] In this section, we specifically discuss the fabrication of HCSN electrocatalysts for fuel cell applications with a detailed analysis of the reported literature.[55–58]

The PEMFC reactions are as follows:[46]

$$\text{Anode: } 2H_2 \rightarrow 4H^+ + 4e^- \quad E^\circ = 0\ \text{V} \qquad (1)$$

$$\text{Cathode: } O_2 + 4H^+ + 4e^- \rightarrow 2H_2O \quad E^\circ = 1.23\ \text{V} \qquad (2)$$

$$\text{Overall: } 2H_2 + O_2 \rightarrow 2H_2O \quad E^\circ = 1.23\ \text{V} \qquad (3)$$

An ultra-thin Pt monolayer (0.025 mg $cm^{-2}$) was deposited on a Pd/C substrate to produce a core–shell catalyst which delivered high performance in PEMFCs due to the higher specific surface area (SA) of Pt (SA, 205–240 $m^2_g$ $Pt^{-1}$) and reduced the cost of the fuel cells.[52] In addition, the costs and

stack sizes of the fuel cells were further reduced by increasing the voltage loss at a high current density (HCD).[52] Karuppannan *et al.* studied the importance of depositing ultra-thin Pt–C layers on C nanofiber (CNF) surfaces by coating with a wet Pt–aniline complex for optimizing the performance of PEMFCs.[59] The carbonization of the prepared material at 900 °C under an $N_2$ atmosphere led to the uniform deposition of 3–4 nm-sized Pt nanoparticles with a thin layer of C on the CNF surface. The Pt@CS-CNF900 electrode had an $E_{1/2}$ value that was 10 mV higher than that of the Pt/C electrode.[59] The electrochemically active surface area (ECSA) values observed for the samples carbonized at 600 (95.6 $m^2_g\ Pt^{-1}$), 700 (100.5 $m^2_g\ Pt^{-1}$), and 900 °C (99.6 $m^2_g\ Pt^{-1}$) indicated the presence of more active sites than in Pt/C. A higher mass activity was observed for the sample that was carbonized at 900 °C (116.7 ± 1 $m^2_g\ Pt^{-1}$) compared to those carbonized at 600 (97.8 ± 1 $m^2_g\ Pt^{-1}$) and 700 °C (90.8 ± 1 $m^2_g\ Pt^{-1}$). The cell voltage decreased from 0.796 to 0.794 V for Pt@CS-CNF900, while that for Pt@CS-CNF600 decreased from 0.799 to 0.754 V.[59] These results proved that the stability and performance were improved by carbonizing the sample at 900 °C.

Lin *et al.* studied the PEMFC application of the synthesized core–shell Co@Pt (1:3)–C electrocatalyst and the heat-treated sample (Co@Pt (1:3)–C (reduced)) obtained at 500 °C under a 5 vol% $H_2/N_2$ gas flow and compared their activities with that of a commercial Johnson Matthey (JM) Pt/C catalyst.[55] The synthesized Co@Pt (1:3)–C electrocatalyst had an average particle size of approximately 3 nm and excellent dispersibility on the electrode. According to the experimental results, the heat-treatment of Co@Pt (1:3)–C that resulted in the formation of Co@Pt (1:3)–C (reduced) significantly enhanced the half-wave potential values (0.803 V and 0.842 V for the former and latter electrocatalysts, respectively) which were comparable to that of the commercial Pt/C catalyst. The Tafel slopes of the (JM) Pt/C, Co@Pt (1:3)–C (reduced), and Co@Pt (1:3)–C electrocatalysts were 74, 78, and 85 mV $decade^{-1}$, respectively. Furthermore, the PEMFC performance of the Co@Pt (1:3)–C (reduced) electrocatalyst was studied in a single cell set-up using the Co@Pt (1:3)–C (reduced) catalyst as the cathode and Pt/C as the anode. Electrochemical impedance spectroscopy (EIS) was performed using (JM) Pt/C and Co@Pt (1:3)–C (reduced) as the working electrodes and Pt/C as the counter electrode under $H_2$ saturation conditions. The ohmic resistances of the (JM) Pt/C and Co@Pt (1:3)–C (reduced) catalysts were 10.1 mΩ and 13.9 mΩ, respectively. The diameters of the kinetic loops for Pt/C (JM) and Co@Pt (1:3)–C (reduced) were determined to be 12 and 12.2 mΩ, respectively.[55] Additionally, the Co@Pt (1:3)–C (reduced) electrocatalyst imparted exceptional stability and durability to the PEMFCs without losing its characteristic properties.

Various CSNs were studied exclusively concerning PEMFC applications.[45,55,60–65] Ahn *et al.* discussed the importance of the Nafion ionomer content for the preparation of Pt/ordered mesoporous C (OMC) electrocatalyst slurries used in PEMFCs.[61] The optimum ionomer contents were found to be ~20 and 30 wt% when carbon black was used as the catalyst support in the HCD region, whereas the use of the Pt/OMC catalyst support required only 10 wt% of ionomer for optimized PEMFC performance (Fig. 4).[61] The gram-scale synthesis of the core–shell structure was performed using a microwave-assisted polyol method on a carbon black support using a CuPt alloy as the core which was encased in a Pt shell. The obtained catalyst delivered high electrochemical activity toward the ORR and demonstrated a high potential for use in PEMFCs.[66] The pyrolysis of Pt@Zn-based ZIF-8 at 800 °C under a mixed gaseous atmosphere of $H_2$ and Ar (1:20) for 5 h afforded N-doped C decorated PtZn intermetallic PtZn@NC.[67] The 10%-PtZn@NC-800 electrocatalyst displayed an increased $E_{1/2}$ value of 0.912 V *vs.* reversible hydrogen electrode (RHE) for the cathodic ORR in an acidic medium compared to that of Pt/C (0.886 V). In addition, the 10%-PtZn@NC-800 electrocatalyst exhibited 3 to 5 times higher mass and specific activities than the commercial

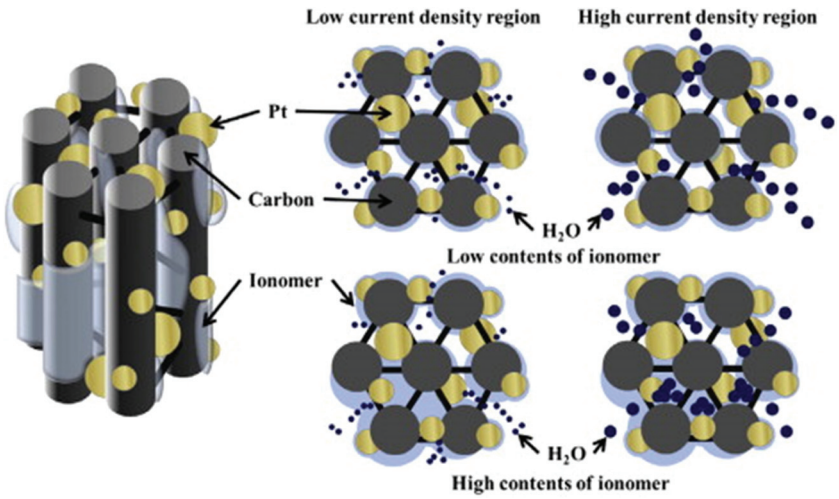


Fig. 4 Schematic illustration of the effect of ionomer contents in the low and high current density regions. Reproduced from ref. 61 with permission from Elsevier B.V.

Pt/C electrocatalyst with excellent stability after 5000 cycles. Moreover, the electrocatalyst exhibited superior activity with respect to methanol and formic acid oxidation reactions. These results suggest the wide applicability of the 10%-PtZn@NC-800 electrocatalyst in PEMFCs.

**2.1.2. HCSNs for anion exchange membrane fuel cells (AEMFCs) and alkaline anion exchange membrane fuel cells (AAEMFCs).** Similar to PEMFCs, AEMFCs play a prominent role in energy conversion owing to the high demand of non-Pt group metals (non-PGM) for reducing the cost and enhancing the durability of fuel cells.[68,69] AEMFCs are less efficient than PEMFCs. Continuous research is being conducted to improve the durability of AEMFCs with respect to long-term operations.[69,70] AEMFCs containing polyolefins and polyaromatic compounds exhibit high power densities.[70] Polyolefin-based AEMFCs have power densities of $\geq$2 W cm$^{-2}$ at 60–80 °C, whereas those based on polyaromatic compounds have power densities $\geq$1.5 W cm$^{-2}$ at 80–95 °C.[70] AEMFCs exhibit diminished stability in alkaline media due to the degradation of the polymer backbone under strongly alkaline conditions, which leads to a reduction in the molecular weight and chain scission.[70,71] The degradation of the polymer backbone and functional groups decreases the ionic conductivity without affecting the mechanical properties of the membrane. However, in some cases, functional group degradation occurs *via* nucleophilic substitution, which increases the brittleness of the membrane.[71] Initially, aryl-ether type polymers were widely used to fabricate AEMFCs. However, aryl-ether polymers lead to diminished performance and durability at high pH due to the degradation of the aryl-ether linkages (C–O–C bonds).[70,72] Aryl-ether functional polymers were thus replaced with polymers having alkyl chains attached to alkali-stable cationic groups and organic compounds containing highly stable cationic functional groups.[70,73]

Several studies were performed on the various aspects of CSNs using different nanomaterial architectures in AEMFCs.[74–77] Recently, highly conducting hydroxide AEM electrolytes have been employed in an alkaline electrolyte-based fuel cell.[74,78–80] AAEMFCs undergo the HOR at the anode, which generates hydroxide anions based on the ORR at the cathode and produces water as the final product at the anode.[79] Extensive separation of electrodes from the AAEM polymeric electrolyte is observed and the particular transport of hydroxide anions from the cathode to the anode facilitates the migration of water from the anode to the cathode without reactant/oxidant gas crossover.[79] Sa *et al.* synthesized CNTs with heteroatom-doped C (HDC) derived from ionic liquids (ILs), such as [1-butyl-3-methylimidazolium bis(trifluoromethylsulfonyl)imide (BMITFSI)], in the presence of tetraethyl orthosilicate (TEOS).[74] The ILs containing N, S, and fluorine (F) in their structures were uniformly deposited on the CNTs through acid reflux, followed by thermal annealing at 800–1000 °C. The CNT/HDC prepared at 1000 °C demonstrated excellent ORR activity with superior kinetic current density and half-wave potential in alkaline media compared to those subjected to other carbonization temperatures and its performance was almost identical to that of commercial Pt/C.[74] In alkaline fuel cells, the CNT/HDC-1000 based MEA exhibited a very high onset potential of 0.85 V, which was superior to that observed in the case of a CNT-based MEA. The power (221 mW cm$^{-2}$) and current density (368 mA cm$^{-2}$) of the CNT/HDC-1000 cathode at 0.6 V in an $H_2/O_2$ atmosphere in an alkaline fuel cell were 23.3 times higher than the corresponding values for the CNT-based cathode.[74] Lee *et al.* prepared cobalt-supported HDC from natural bean sprouts as a biosource that absorbed the metal precursor. The material was subsequently carbonized at 900 °C for 2 h at a heating rate of 10 °C min$^{-1}$ under an Ar atmosphere.[75] The prepared electrocatalyst delivered outstanding ORR activity in alkaline media due to the presence of heteroatoms and a large surface area. The heteroatom-doped electrocatalyst had a higher positive half-wave potential value (0.836 V) than a metal-supported C electrocatalyst devoid of heteroatoms (0.767 V), C derived from bean sprouts (0.683 V), and a commercial Pt/C electrocatalyst (0.825 V). Furthermore, the cobalt supported HDC electrocatalyst exhibited a high power density of 172.2 mW cm$^{-2}$ at 0.373 V in AEMFCs.[75]

Woo *et al.* synthesized P- and S-doped Fe–N/C electrocatalysts by a silica coating mediated method, which delivered an excellent ORR performance with a half-wave potential of 0.91 V *vs.* RHE in alkaline media.[76] The P- and S-doped Fe–N/C electrocatalysts also exhibited higher current densities of 904 and 977 mA cm$^{-2}$ at 0.6 V compared to the undoped Fe–N/C electrocatalyst which showed a current density of 669 mA cm$^{-2}$ at 0.6 V (Fig. 5(a)).[76] The introduction of heteroatoms to the undoped Fe–N/C electrocatalyst enhanced the half-cell activity in both the rotating disc electrode and single-cell performance tests (Fig. 5(b)).[76] The S-doped Fe–N/C electrocatalyst exhibited a power density of 635 mW cm$^{-2}$ in AEMFC applications with a markedly improved MEA performance in both acidic and alkaline electrolytes.

A carbide-derived C material co-doped with a transition metal and N (M/N/CDC) was prepared by reacting titanium carbide-derived C with dicyandiamide in the presence of ferric chloride ($FeCl_3$) or cobalt chloride ($CoCl_2$) as the dopant.[81] The MEA of the obtained M/N/CDC cathode delivered an excellent power density of 80 mW cm$^{-2}$ compared to the Pt/C cathode (90 mW cm$^{-2}$). Dekel *et al.* briefly reviewed the various aspects of hydrogen-fueled AEMFCs, Pt-free hydrogen AEMFCs, and the stability of hydrogen AEMFCs.[82] AEMFCs are used under alkaline conditions, whereas acidic conditions are applied in PEMFCs. The hydroxide anions migrate from the cathode to the anode *via* the AEMs in AEMFCs which is analogous to the $H^+$ conduction pathway in PEMFCs.[82] AEMs function as solid electrolytes which conduct hydroxide and carbonate anions owing to the presence of positively charged cationic groups on their polymer backbone.[82] An Fe–tin (Sn) C nitride graphene core–shell electrocatalyst prepared at 900 °C delivered an ORR overpotential of ~70 mV, thus demonstrating potential utility in AEMFCs.[83]

Recently, AAEMFCs have been applied more extensively in fuel cell technology compared with AEMFCs and PEMFCs because they are capable of performing the selective transport of hydroxide ions from the cathode to the anode *via* a membrane.[79,84–86] Thin membranes derived from solid polymer electrolytes are used in AAEMFCs. However, the presence of carbonate anions diminishes the ionic conductivity of the

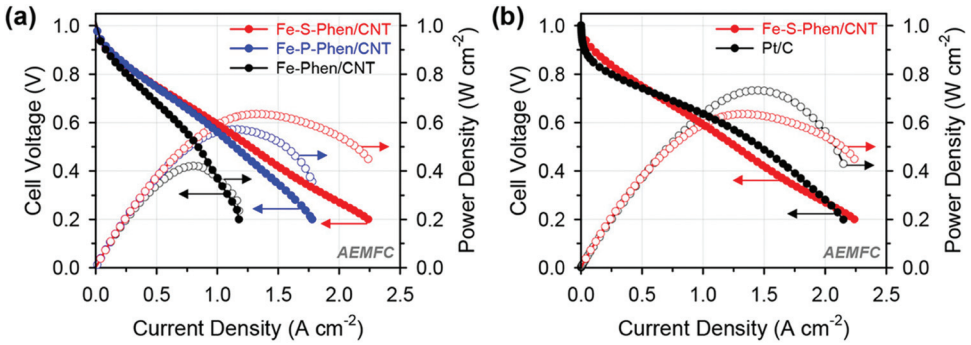


Fig. 5 Alkaline AEMFC performance of MEAs using (a) Fe-Phen/CNT, Fe-P-Phen/CNT, and Fe-S-Phen/CNT as cathode catalysts and (b) Fe-S-Phen/CNT and Pt/C as cathode catalysts. Reproduced from ref. 76 with permission from the American Chemical Society.

membranes over time, which is a major issue.[84] Polymer electrolytes also suffer from low ion exchange conductivity (IEC). Polymer electrolytes with improved IEC and stable mechanical properties are necessary to achieve efficient AAEMFC activity. Various AEMs have been prepared using different types of polymer backbones and functional ionic groups for successful use in AAEMFCs. We have listed some of the important CSN and HCSN based catalysts and their results using AEMFCs and AAEMFCs (Table 1).

**2.1.3. HCSNs for direct methanol fuel cells (DMFCs).** DMFCs are integral to fuel cell technology due to the associated advantages of high energy density (arising from the presence of alcohols: methanol and ethanol), low cost, environmental friendliness, and ease of use.[42,98–100] Moreover, DMFCs generate electricity without using fossil fuels and can function at low temperatures. Additionally, they are amenable to swift refueling techniques and do not require electricity for recharging. However, DMFCs have certain disadvantages, such as the methanol crossover effect in PEM, high cost, and difficulties in maintaining durability and stability as well as controlling the heat and water output. In addition, low reaction rates are observed at the cathode and anode during oxygen reduction and methanol oxidation, respectively. Several other factors require consideration while developing DMFCs, such as the loading of the catalyst, power density, configuration of the diffusion layer, assembly of the membrane electrode, and membrane thickness.[98] According to some studies, high methanol conversion rates were achieved in DMFCs by increasing the catalyst loading.[101,102] However, this necessitates a higher loading of Pt on the electrode which increases the cost of the electrocatalyst and facilitates methanol crossover due to the poor tolerance of Pt against alcohols.

Table 1 Comparison of various CSNs and HCSNs and their results in AEMFCs and AAEMFCs

| Catalyst | Membrane | Loading density (mg cm$^{-2}$) | OCV (V) | Maximum power density (mW cm$^{-2}$) | Ref. |
|---|---|---|---|---|---|
| CNT-HDC-1000 | — | 2.0 | — | 270 | 74 |
| NBSCP | FAA-3 | 3.0 | 1.01 | 172 | 75 |
| CoMn-pNGr | FAA-3 | 2.0 | 0.92 | 35.20 | 87 |
| Fe–Co-NpGr | FAA-3 | 2.5 | 0.85 | 35 | 88 |
| Fe–N-comp-0.5 | A201 | 2.6 ± 0.2 | 0.92 | 160 | 89 |
| Fe-M-La-C-700 | A201 | 4.0 | 0.64 | 137 | 90 |
| Fe-NMG | A201 | 3.5 | 1.05 | 218 | 91 |
| Fe-NMG-35 wt% | A201 | 3.5 | — | 218 | 91 |
| Fe–N–C (1000 °C) | aQAPS-$S_8$ | 2.0 | — | 485 | 92 |
| Fe–N–C (800 °C) | aQAPS-$S_8$ | 2.0 | — | 450 | 92 |
| AT-FeNC | aQAPS-$S_8$ | 4.0 | — | 164 | 93 |
| FeCoN-C-HLH | Tokuyama A-201 | 4.0 | — | 177 | 94 |
| N-CNT | — | 5.0 | — | 37 | 95 |
| NCNHs | Fumapem FAA | 3.0 | 0.75 | 30 | 96 |
| Fe-NCNH-900 | Fumapem FAA | 4.0 | 0.83 | 35 | 97 |

OCV: open-circuit voltage, CNT-HDC-1000: carbon nanotube/heteroatom-doped carbon, NBSCP: $Co_2P$ nanoparticles supported on heteroatom-doped carbon catalysts, CoMn-pNGr: CoMn alloy oxide nanoparticles on N-doped porous graphene, Fe–N-comp-0.5: nitrogen doped iron containing carbide-derived carbon (Fe–N-CDC) and multi-walled carbon nanotubes (MWCNTs), Fe-M-La-C-700: pyrolyzed iron melamine lipoic acid carbon composite at 700 °C, Fe-NMG: iron containing nicarbazin, methylimidazole, and glucoril, Fe–N–C (1000 °C): Fe-containing N-doped carbon, AT-FeNC: aminothiazole derived Fe-containing N-doped carbon, CoFeN–C-HLH: cobalt and iron containing N-doped carbon [HLH: (pyrolyzed:acidic treatment:pyrolyzed)], NCNHs: nitrogen-doped single-walled carbon nanohorns, Fe-NCNH-900: single-walled carbon nanohorns by simultaneous doping with Fe and N at 900 °C.

The Pt electrodes in DMFCs also degrade the catalyst through the formation of carbon monoxide (CO) by the electro-oxidation of methanol, which diminishes the performance.[98] These disadvantages are addressed by mixing Pt with other noble metals, transition metals, or metal oxides which help maintain the stability and tolerance of the electrodes against alcohol while mitigating the effects of CO poisoning.[102] The performance and stability of the electrocatalysts in DMFCs are also enhanced by using porous materials to support the catalytic materials.[103,104] The porous materials are required to possess high surface areas and appreciable electrical conductivity. Additionally, they should facilitate catalyst recovery with repeated cycles, interact strongly with the catalysts, and have superior corrosion resistivity.[105] Yuda *et al.* briefly reviewed the different synthetic pathways for preparing graphitic carbon nitrides (g-$C_3N_4$) and their structural characteristics. The effects of incorporating non-metals and noble and non-noble metals in g-$C_3N_4$ structures on the methanol oxidation reaction (MOR) were discussed along with the applications of these materials in DMFCs.[99] The doping of g-$C_3N_4$ with heteroatoms or metals improved their electrocatalytic performance with respect to DMFC applications.[99,106–108]

Various metals and metal–C based hybrid CSNs, such as Ni–Pd, Ru–Pt, Se–Ru, Au–Pd, Au–PdAg, Au–PtCu, PdCuM (M = Ru, Rh, and Ir), PdCu@Pt, $Pt_3Co$–Pt, PtCuCo, $NiCoO_4$-MWCNTs, and $CeO_2$–rGO–Pt, were used for DMFC applications.[109–120] Jin *et al.* designed trimetallic alloy nanosheet (PdCuRu, PdCuRh, and PdCuIr) based electrocatalysts and studied their electrocatalytic behavior toward the MOR. The synthesized $Pd_{59}Cu_{33}Ru_8$ nanosheets exhibited outstanding mass (1660.8 mA $mg^{-1}$) and specific activities (4.7 mA $cm^{-2}$), which were 4.9- and 2.8-fold higher than those of the other trimetallic alloys and the Pd/C catalyst, respectively.[115] Parthiban *et al.* studied the role of sulfonic acid-functionalized graphene (SFG) in conjunction with proton-conducting Nafion in controlling the methanol crossover effect in DMFCs.[121] The material delivered superior electrocatalytic activity and the combination of SFG and Nafion reduced the extent of methanol crossover compared to that observed in the presence of pristine Nafion (Fig. 6(a)).[121] In addition, the functionalized material retained its stability after 50 h of operation owing to its considerably low methanol permeability (Fig. 6(b)).[121] The obstruction to the methanol pathway caused by the binding of S-graphene on the polymer membrane is responsible for the lower methanol diffusivity of the material.

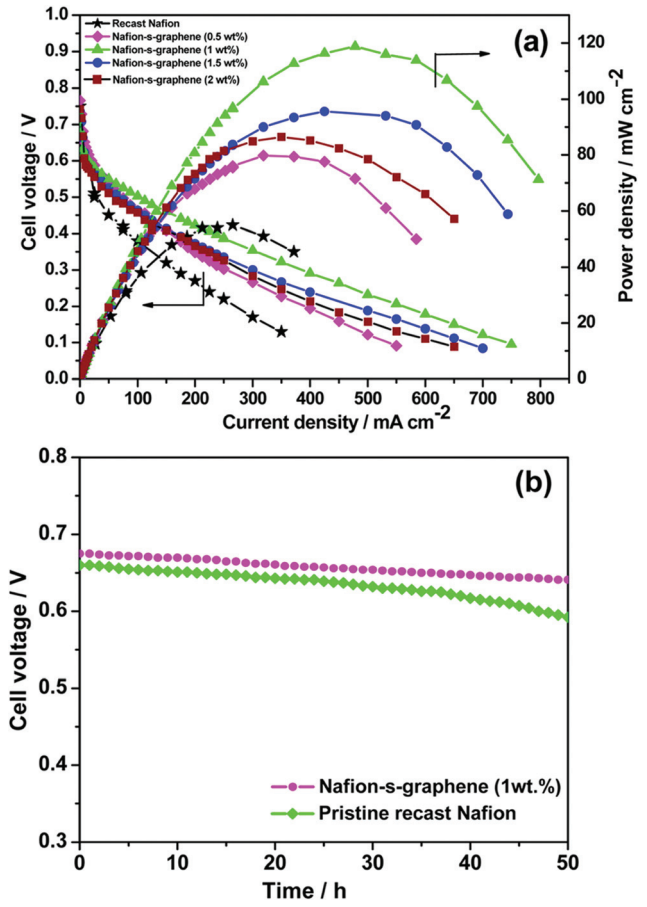


Fig. 6 (a) DMFC performance of pristine Nafion and Nafion–S-graphene hybrid membrane at 70 °C under ambient pressure. (b) Stability test of the membranes for 50 h under fuel cell configuration at OCV. Reproduced from ref. 121 with permission from the American Chemical Society.

The DMFC polarization and performance curves indicate that the hybrid membranes have considerably higher open-circuit voltages (OCVs) at 70 °C under ambient pressure than the pristine Nafion membrane, which indicates a lower extent of methanol crossover in the presence of the hybrid membrane (Fig. 6(a)).[121] The hybrid membrane prepared using 1 wt% S-graphene exhibited an outstanding power density of 118 mW $cm^{-2}$ which was considerably higher than those recorded for the pristine Nafion membrane (54 mW $cm^{-2}$) and the other hybrid membranes containing different proportions of S-graphene. The sulfonic acid functional group present in the hybrid membrane has excellent proton-conducting characteristics and enhances the power stability, making the hybrid membrane highly suitable for DMFC applications (Fig. 6(b)).[121] The conductivity of the membrane was partially reduced upon increasing the S-graphene content as the ionic conducting pathways were hindered.[121] Moreover, a reduction in the extent of methanol crossover was reported upon using the sodium dodecyl sulfate (SDS) surfactant as a template to develop a porous C-Nafion membrane.[122]

Çögenli *et al.* synthesized an N and B doped 3D porous graphene aerogel, followed by Pt loading on the material by a microwave heating method.[123] The obtained heteroatom-doped materials demonstrated superior catalytic activity in both formic acid and methanol oxidations.[123] A highly stable and methanol tolerant electrocatalyst was also developed by applying the core–shell technique to C nanofibers using Pt cores and C shells in the presence of aniline. The electrocatalyst was found to be highly effective in DMFC applications.[124] In Table 2, we outlined the important results of DMFCs such as methanol concentration with respect to a power density of the CSN based catalyst. To the best of our knowledge, there are very few studies on the role of heteroatom doping and CSNs in DMFC applications. Detailed studies are extremely necessary to understand the importance of CSNs and HCSNs in enhancing the electrocatalytic performance of DMFCs.

**2.1.4. HCSNs for microbial fuel cells (MFCs).** MFCs involve a bio-electrochemical technique that is more eco-friendly and sustainable compared to other fuel cell applications.[125] Recently, single chamber MFCs (SCMFCs) have attracted considerable attention due to their low cost and operational simplicity.[25] MFCs mainly utilize electroactive bacteria which consume organic matter and produce bioelectricity.[131] During the MFC operation, electrons and protons are liberated from the anode due to the oxidation of organic pollutants or substrates by electro-active bacteria and pass through an electron circuit and a PEM to the cathode, generating bioelectricity.[131,132] Li *et al.* synthesized N doped carbonaceous transition metal electrocatalysts, such as CoN–C, MnN–C, and CuN–C, by the hydrothermal method using melamine as an N source and formaldehyde as a C source.[25] The MFC performance was estimated in a plexiglass reactor equipped with an anode chamber and an air cathode fabricated on a C cloth using the synthesized catalyst. Carbon felt was used as the anode material and the anode medium consisted of bacteria, sodium acetate, phosphate buffer solution, vitamins, and mineral solutions.[25] PEM was used as a separator

Table 2 The results of various CSN based catalysts for DMFCs

| Catalyst | Methanol concentration (M) | Power density (mW $cm^{-2}$) | Ref. |
|---|---|---|---|
| Au–$Ag_2S$–Pt nanocomposites | 0.5–15 | 89.7 | 125 |
| Hydrophobic anode MPL | 8 | 78 | 126 |
| Modified-anode MPLs | 5 | 77.9 | 127 |
| Modified-anode MPLs | 7 | 67.7 | 127 |
| Poly(SHS-ddm) | 7 | 66.5 | 128 |
| GO nanoplatelets | 5–10 | 50 | 129 |
| PMFSP | 2–4 | 7 | 130 |

Au–$Ag_2S$–Pt: gold and silver sulfide core–shell decorated with platinum, modified-anode MPLs: the combination of commercial carbon black (CB, (50 vol%)) and platelet carbon nanofibers (PCNFs, (50 vol%)) with a micro-porous layer, poly(SHS-ddm): cross-linked sulfonic acid-containing polybenzoxazine, PMFSP: porous metal fiber sintered plate.

for both the anode chamber and air cathode. During the ORR, the CoN–C electrode exhibited superior electrocatalytic activity to the MnN–C, CuN–C, and N–C electrodes. This was due to the high availability of oxygen vacancies and pyridinic-N species, which enhanced the rate of electron transfer, kinetic activity, and ECSA and delivered a higher exchange current density and power density.

Yang *et al.* prepared a bio-waste derived catalytic material by carbonizing the anaerobic digestion products of *Broussonetia papyrifera* at 800 °C for 2 h under an $N_2$ atmosphere at a heating rate of 5 °C $min^{-1}$.[133] N doped C (N–C) and Fe and N co-doped C (Fe–N–C) were also produced in the absence and presence of ferric chloride ($FeCl_3$) at 800 °C under an $N_2$ atmosphere for 2 h (Fig. 7(A)).[133] The prepared Fe–N–C electrode displayed excellent ORR activity due to the formation of active Fe–N–C sites which facilitated the transfer of electrons and protons. In addition, the enhanced formation of graphitic structures in the catalyst increased its conductivity. The Fe–N–C catalyst exhibited appropriate adsorption of oxygenates (*O, $*O_2$, *OH, and *OOH), which led to the enhancement of the ORR activity.[133] Furthermore, the Fe–N–C electrode, when used in MFCs, dispatched a maximum power density of 1308 mW $m^{-2}$ which was superior to that recorded in the case of the N–C electrode (638 mW $m^{-2}$). The open-circuit potentials of the Fe–N–C, Pt/C, and N–C catalysts in the MFCs were found to be 0.63, 0.62, and 0.47 V, respectively (Fig. 7(B)).[133] In addition, the Fe–N–C catalyst exhibited outstanding activity in the MFC after 500 cycles of operation due to the presence of a large specific surface area and a high number of active sites, which were responsible for the excellent stability of the catalyst.[133] Luo *et al.* prepared an ordered mesoporous C (Fe–N–C) material containing atomically dispersed Fe–$N_x$ active sites derived from MOFs.[134] The developed material had excellent properties, such as high values of maximum power density (1232.9 mW $m^{-2}$), constant output voltage (0.46 V), and open-circuit voltage (0.644 V). These values established that the developed materials had considerably superior catalytic properties to 20% Pt/C in MFCs.[134] The presence of active Fe–$N_x$ sites and pyridine- and graphite-like N structures is responsible for enhancing the catalytic activity in MFCs. Various types of Fe–N–C based materials have been widely used in MFCs.[135–139] In addition, various core–shell-based electrocatalysts fabricated using heteroatom-doped transition metals have been studied with respect to MFCs.[25,140–144] The catalytic activity of different HCSNs in MFCs is also presented in Table 3.

**2.1.5. HCSNs for other fuel cells.** HCSN based materials are used in various other types of fuel cell applications such as urea- and formic acid-based fuel cells. Direct urea fuel cells (DUFCs) are a type of fuel cell which typically consumes wastewater containing urea/urine as a fuel and low-cost or noble metals as catalysts. The overall performance of a DUFC depends on the OER and ORR performances of the catalyst. The development of a single electrocatalyst with dual OER and ORR properties for DUFCs is highly challenging because of the disadvantages associated with maintaining the stability of the electrocatalyst. Recently, several attempts have been made to improve the stability of the electrocatalysts for DUFC applications using various low-cost transition metals such as Ni, Co, and Mn *via* the CSN technique since CSNs offer some unique properties.[157,158] Senthilkumar *et al.* studied the effective role of transition metal oxide (NiO and MnO) coatings on $Co_3O_4$ nanowire loaded C cloth in forming 3D hierarchical CSNs with bifunctional electrocatalytic properties suitable for DUFC applications. The obtained electrocatalyst displayed an outstanding power density of 22.8 mW $cm^{-2}$ with high durability and stability, as evidenced by the undiminished performance after 120 h of operation.[158] Moreover, such systems are highly important for the sustainable conversion of human waste to value-added products. The DUFC performance of a catalyst mainly depends on the ORR and urea oxidation reaction (UOR). Additionally, the wide applicability of CSNs and HCSNs in direct formic acid-based fuel cells (DFAFCs), similar to other types of fuel cells, has also been demonstrated.[159–162]

Cao *et al.* investigated the applications of ultra-small Ag@Pd CSNs coated on Vulcan XC72R carbon support in DFAFCs. Ag/C nanocrystals were prepared by mixing silver nitrate and Vulcan XC72R carbon with ammonium hydroxide and formaldehyde.[159] The synthesized Ag/C nanocrystals were subsequently modified by doping with palladium chloride in the presence of ethylenediaminetetraacetic acid (EDTA) disodium salt at 160 °C. Ag–Pd–C CSNs of three different compositions were prepared using different Ag/Pd atomic ratios: Ag–Pd–C-1 (63:37), Ag–Pd–C-2 (44:56), and Ag–Pd–C-3 (19:81). The formic acid oxidation reaction (FAOR) was performed using the prepared Ag–Pd–C CSNs. The mass-specific activities (MSA) at a potential of 0.345 V of the three samples were 1.06, 1.47, and 0.84 mA $\mu g^{-1}$, respectively.[159] The MSA of Pd–C and commercial Pd black were found to be 1.04 mA $\mu g^{-1}$ and 0.49 mA $\mu g^{-1}$, respectively. According to these results, of all the materials tested, the Ag–Pd–C-2 CSNs exhibited the highest electrocatalytic activity. In addition, the Ag–Pd–C-2 CSNs exhibited a superior current density (0.124 mA $\mu g^{-1}$) to Pd–C (0.084 mA $\mu g^{-1}$) and Pd black (0.083 mA $\mu g^{-1}$) after 2000 s.[159] The multi-walled carbon nanotube (MWCNT)-supported Ru–Pd CSNs synthesized by Zhang *et al.* also manifested superior FAOR and ethanol oxidation reaction (EOR) properties.[160] The FAOR activities of the synthesized Ru–Pd-MWCNT and Pd-MWCNT materials corresponded to forward peak current densities of 1757 and 976 mA $mg^{-1}_{Pd}$, respectively. Likewise, on examining the EOR activities of the Ru–Pd-MWCNT, Pd-MWCNT, and Pd–C samples, the peak current densities were

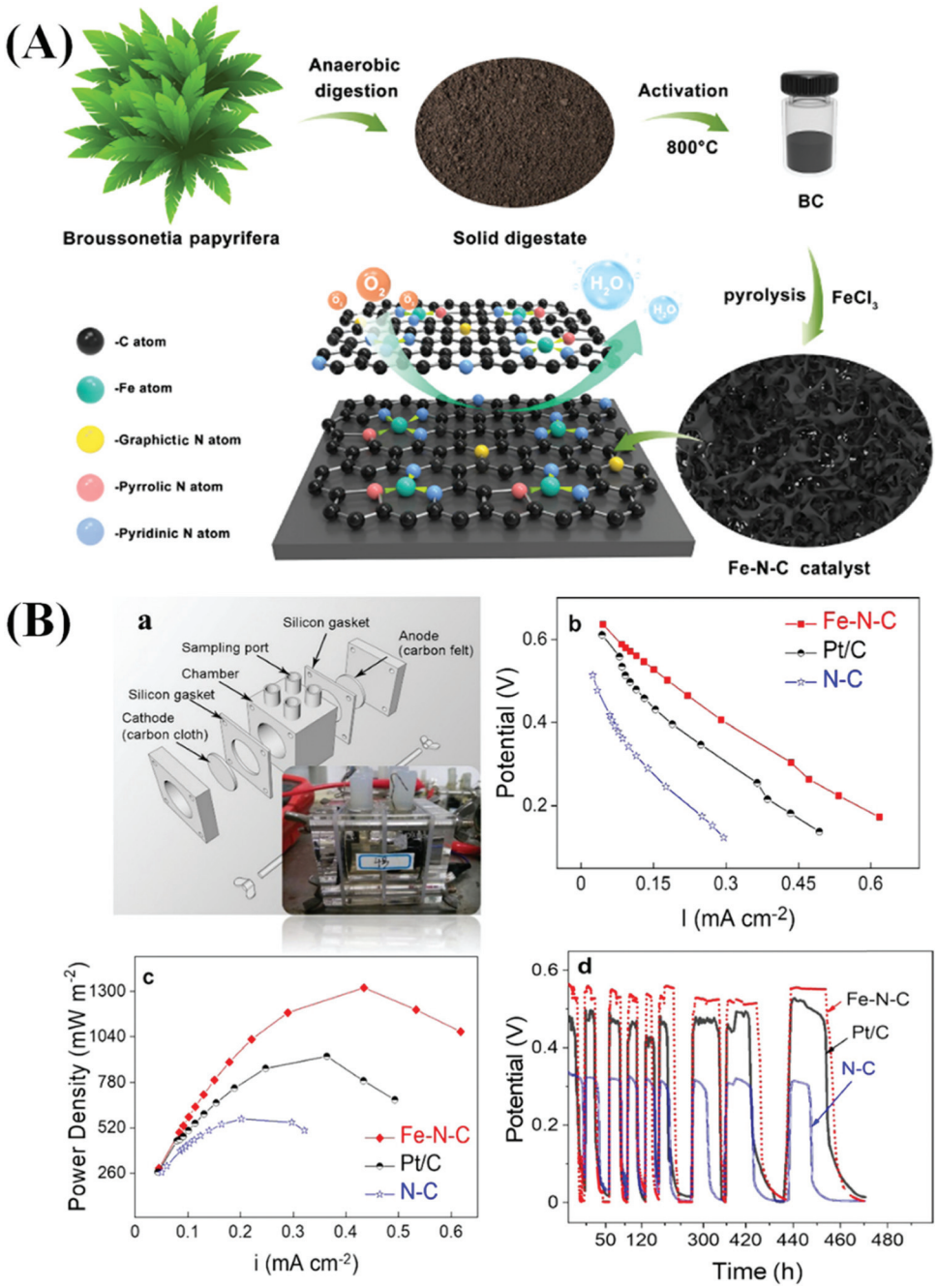


Fig. 7 (A) Schematic illustration of the fabrication of hierarchical Fe–N–C catalysts derived from the solid digestate. (B) Schematic illustration of a single-chamber MFC (a); power density (b) and electrode polarization curves (c), and the periodic variation of single-chamber MFCs coupled with the Fe–N–C, Pt/C, and N–C catalysts (d). Reproduced from ref. 133 with permission from the American Chemical Society.

found to be 2507.5, 1378.2, and 943.5 mA $mg^{-1}_{Pd}$, respectively.[160] The obtained results demonstrate the superior electrochemical activity of the Ru–Pd-MWCNT material toward the FAOR and EOR compared to Pd-MWCNT and Pd–C.[160] $Pt_3Pb$ nanocrystals encased in Pt CSNs also exhibit a higher FAOR activity compared to the nanocrystals devoid of Pt.[161]

### 2.2. HCSNs for metal-ion batteries

Metal-ion batteries are a promising technology related to ECS systems.[34] Metal-ion batteries principally require high specific power and energy densities along with sufficient operational stability. Metal-ion batteries employ polymeric cathodes, such as *N*,*N*′-substituted dihydrophenazine and hexaazatrinaphthylene, and NaK alloy anodes impregnated in C cloth.[163] PAN equipped with organic cyclic chains is used as an effective anode material for metal-ion batteries in alkaline media, exhibiting a reversible capacitance of 1238 mA h $g^{-1}$ under a current density of 50 mA $g^{-1}$.[164] Likewise, organic electrodes featuring carbonyl and disulfide linkages, and those obtained *via* superlithiation, azo and anion insertion, and imine reactions

Table 3 The maximum power density obtained by the use of various HCSN catalysts in MFCs

| Catalyst | Maximum power density (mW $m^{-2}$) | Ref. |
|---|---|---|
| CoN–C-5 | 1202.3 | 25 |
| Fe–N co-doped GNR-CNT | 801 | 136 |
| Fe–N–C-50 | 1166 | 137 |
| NB-CPs | 642 | 141 |
| CP-M-Z | 2288 ± 30 | 142 |
| NP-C | 2293 ± 50 | 145 |
| FePc-CS500 | 2160 ± 20 | 146 |
| Fe–N–C-G | 1601 | 147 |
| Fe–N–C | 1620 ± 30 | 148 |
| Fe–N-HCN | 1300 ± 64 | 149 |
| Co-Co9S8-NPGC | 1156 ± 18 | 150 |
| Fe–N-AC | 1092 | 151 |
| N-CA | 967 ± 34 | 152 |
| Fe–C-Ns-900 | 900 | 153 |
| NFe-CNS | 866.5 ± 7 | 154 |
| FePc-PID-CNTs | 799 | 155 |
| NPOMC | 245.8 | 156 |

Note: NP-C: N and P dual-doped carbon from cellulose, CP-M-Z: magnesium and zinc containing pyrolyzed carbon, FePc-CS500: iron(II)-phthalocyanine containing macroporous hollow nanocarbon shells, Fe–N–C-G: iron–nitrogen–carbon nanorod network-anchored graphene nanohybrid, Fe–N–C: Fe–N-doped carbon, Fe/N-HCN: Fe–N-doped porous hollow carbon nanospheres (HCNs), Co–$Co_9S_8$-NPGC: nitrogen-doped Co–$Co_9S_8$-partly-graphitized carbon, Fe–N-AC: iron–nitrogen/activated carbon, N-CA: N-doped carbon aerogel, Fe–C-Ns-900: Fe-containing N-doped carbon, NFe-CNS: nitrogen and iron co-doped carbon nanospheres, Fe–N co-doped GNR-CNT: iron, nitrogen co-doped graphene nanoribbon-carbon nanotube, FePc-PID-CNTs: iron phthalocyanine and polyindole on carbon nanotubes/carbon Vulcan, NB-CPs: nitrogen and boron-*co*-doped core–shell carbon nanoparticles, NPOMC: nitrogen- and phosphorus-doped ordered mesoporous carbon.

have been used in metal-ion batteries.[165] Various HCSNs have been used for improving the performances of metal-ion batteries due to their efficient electrocatalytic properties and highly controlled architectures. Herein, we briefly describe the different HCSNs used for the development of metal-ion batteries such as Li, sodium (Na), and K-ion batteries.

**2.2.1. HCSNs for Li-ion batteries (LIBs).** Li-ion batteries (LIBs) constitute one of the most important research topics of the present decade. The 2019 Nobel Prize in Chemistry was awarded for advances in research related to LIBs. LIBs offer an alternative approach for generating renewable energy storage systems which are more desirable than conventional energy storage systems produced using fossil fuels, coal, and thermal sources.[166] LIBs are highly advantageous for use in electronic vehicles and portable electronic devices because they are flexible, lightweight, and stable.[167] Research is focused on the development of lightweight and inexpensive LIBs having higher energy densities, smaller sizes, and enhanced life cycles to ensure superior performance and wide applicability.[166,168] Several approaches have been adopted to fabricate LIBs. Recently, there have been several reports on the application of CSNs and HCSNs for LIB fabrication due to their advantageous properties, which include controlled porosity, high surface area, tunability of the core and shell compositions, and retention of the structural integrity and stability after multiple cycles of use.[166,169–178] Liu *et al.* commenced their investigation of N-heteroatom doped multi-CSNs by synthesizing highly uniform $Mn_3O_4$ nanoparticles by a hydrothermal method in a Teflon-lined stainless-steel autoclave at 80 °C for 2 h. Subsequently, polymerization was performed along with the growth of the shell structure on $Mn_3O_4$ nanoparticle cores using dopamine (DA) while stirring at room temperature for 24 h, followed by drying at 100 °C for 12 h (Fig. 8).[177] The obtained $Mn_3O_4$–polydopamine (PDA) CSNs were then subjected to heat treatment at 600 °C for 3 h under an $N_2$ gas flow at a heating rate of 5 °C $min^{-1}$. The nanoparticles are named $MC_NC_mSPs$ (also known as MnO multi-core-N-doped C shell nanoparticles). PDA plays the dual role of supplying C and N atoms and forming microporous structures, which enhances the electrical conductivity of the C shell and facilitates electron transfer to the core material. When used in a LIB, the carbonized PDA electrocatalyst exhibited an initial specific capacitance of approximately 1490 mA h $g^{-1}$ at a current density of 100 mA $g^{-1}$, which dropped to 578 mA h $g^{-1}$ after 60 cycles, indicating good stability, excellent rate capability, and coulombic efficiency of the anode catalyst.[177]

Zhou *et al.* also studied the LIB behavior of heteroatom-doped core–shell carbonaceous framework materials derived

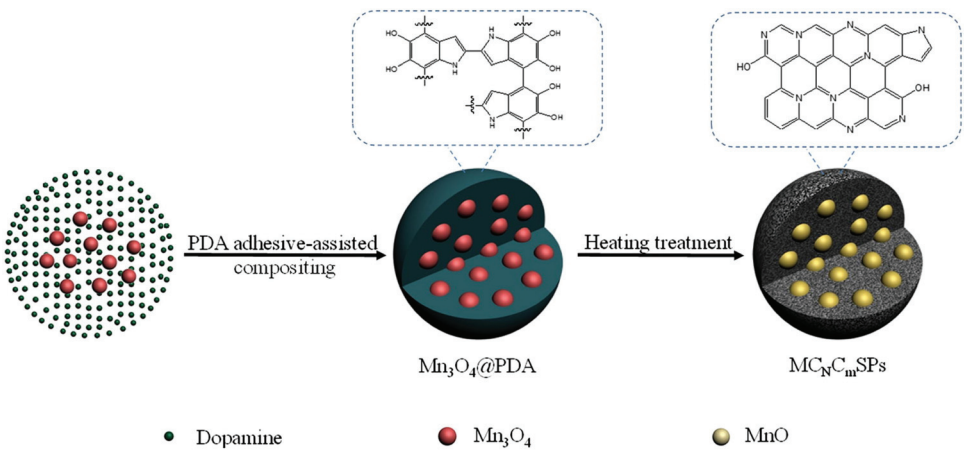


Fig. 8 Schematic illustration of the fabrication of MCNCmSPs by a PDA adhesive-assisted compositing procedure. Reproduced from ref. 177 with permission from Elsevier Ltd.

from ZIF-8 and cyclomatrix poly(organophosphazenes) (POPs).[22] Li-ions and atoms have apertures sizes of ~1.5 Å and 3.0 Å, respectively, whereas ZIF-8 has apertures measuring ~3.4 Å. These values demonstrate the excellent potential for interaction and migration of Li-ions and atoms in ZIF-8 networks and the feasibility of their application in LIBs. POPs are composed of organic–inorganic hybrid frameworks with intrinsic heteroatoms such as P, S, N, and O and covalently cross-linked polymer backbones.[22] The size of the synthesized POP nanosphere core is around 200 nm and that of the ZIF-8 shell is in the range of 50 to 300 nm. The POP-ZIF-8 material has an approximate surface area of 1557 $m^2$ $g^{-1}$. The POP-ZIF-8 materials contain transition metals, such as Zn, and heteroatoms such as P, N, and S. In addition, the carbonization of the POP-ZIF-8 material leads to the formation of core@shell heteroatom-doped carbonaceous structures. The LIB efficiency of the material was examined using the coin cell approach over a series of charge and discharge cycles at cell voltages of 0.01 and 2 V *vs.* $Li/Li^+$ and a current density of 74 mA $g^{-1}$. The POP-ZIF-8 synthesized using 1 : 2.5 and 1 : 8 weight ratios have initial charge capacities of 493 and 580 mA h $g^{-1}$, and discharge capacities of 538 and 647 mA h $g^{-1}$, respectively.[22] An increase in the capacity was observed upon increasing the POP-ZIF-8 weight ratio due to the abundance of heteroatoms and metals, which generated more reactive sites for the pseudo-redox reactions. Moreover, the obtained results suggest that an increase in the proportion of ZIF-8 results in an increase in the anode capacity and stability, which enhances the anode reactivity toward the lithiation and de-lithiation steps in LIBs.

Hua *et al.* explained the mechanism of the (de)lithiation process in the core–shell NCM electrode during the first cycle (Fig. 9).[179] Lithium ions are first taken from the Ni-rich core phase, which has a higher concentration of reactive Ni, due to the microscopic open pores of the core–shell NCM material. Because the initial charge of the Mn-rich phase is smaller than that of the Ni-rich phase, the state of charge of the shell controls the electrochemical properties of the core–shell NCM.

**2.2.2. HCSNs for sodium-ion batteries (SIBs).** SIBs and LIBs share many similarities due to the similar physical and chemical properties of Na to Li (both have a high redox potential of 0.3 V). The development of SIBs is facilitated by the abundant availability of Na in the earth's crust. In addition, SIBs are inexpensive and have low toxicity.[180–185] However, SIBs suffer from large diffusion resistance owing to the larger ionic radius and molar mass of $Na^+$ compared to $Li^+$.[186] This disadvantage can be addressed by designing SIBs with high energy and power densities and long lifetimes.[183] Recently, transition metal chalcogenides (TMCs), such as metal oxides, selenides, and sulfides, have been widely used for enhancing the energy density of LIBs owing to their remarkably high theoretical capacities and activities and robust structures.[181,183,184,186–188] CSNs containing two different transition metals can mitigate the disadvantages associated with carbon-coated CSNs.[189] The Na-ion storage properties of metal oxides can be improved by controlling their morphology such that the surface area and a number of active sites are enhanced. Such modifications facilitate ion intercalation, promoting the transfer kinetics of Na ions.[190] Zhao *et al.* synthesized $FeS_2$, $FeSe_2$, and $FeS_2$–$FeSe_2$ CSN electrodes and studied their Na storage capabilities.[189] Among these electrodes, $FeS_2$–$FeSe_2$ exhibits the highest retention of discharge capacity (395 mA h $g^{-1}$ at 1 A $g^{-1}$) after 270 cycles. On the other hand, the $FeS_2$ and $FeSe_2$ electrodes exhibit reversible capacities of 62 and 155 mA h $g^{-1}$, respectively. The discharge capacity values of the $FeS_2$–$FeSe_2$ electrode were 350 and 301.5 mA h $g^{-1}$ after 2700 (at 1 A $g^{-1}$) and 3850 (at 5 A $g^{-1}$) cycles, respectively. Additionally, the electrode maintained a coulombic efficiency of almost 98 to 100%. Heteroatom-doped CSNs have been successfully applied in SIBs. Bai *et al.* investigated the utility of N-doped C coatings on anatase $TiO_2$ in SIBs.[191] Anatase $TiO_2$ is a positive metal oxide anode material that facilitates the diffusion of Na ions. The *in situ* polymerization of anatase $TiO_2$ with PDA, followed by pyrolysis, leads to the formation of an N-doped C coating on the CSNs with an abundance of oxygen vacancies.[191] The $TiO_{2-x}$-NC core–shell nanospheres when used as anodes for SIBs delivered an outstanding rate capability and reversible

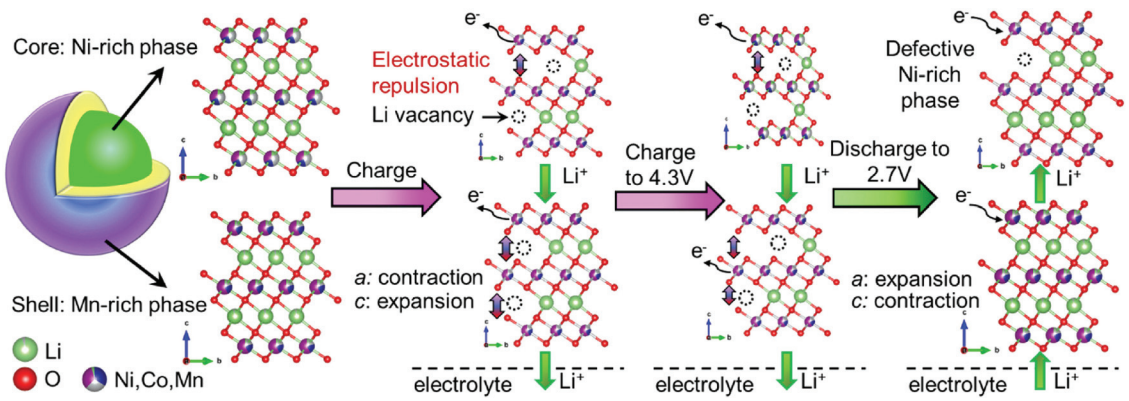


Fig. 9 Schematic illustration of a subsequent (de)lithiation mechanism in the core–shell NCM cathode materials during the first cycle, showing an obvious change in the unit-cell volume of the Ni-rich phase within the interior region of a secondary particle with respect to the Mn-rich phase. TM: Ni – whitish; Mn – magenta; Co – blue. Reproduced from ref. 179 with permission from the Authors, Elsevier Ltd.

capacity of 245.6 mA h $g^{-1}$ at 0.1 A $g^{-1}$ after 200 cycles which was due to the presence of a high number of oxygen vacancies and N-doping, which improved the electronic and ionic conductivity.

**2.2.3. HCSNs for potassium (K)-ion batteries (KIBs).** KIBs are attractive metal-ion batteries because of their excellent performance and low cost. Additionally, the abundant availability of K facilitates the development of large-scale energy storage devices.[192–194] However, a key bottleneck for KIBs is the requirement of highly stable cathode materials owing to their rigid frameworks. Some other notable disadvantages include the larger size of $K^+$ (1.38 Å), as compared to $Na^+$ (1.02 Å) and $Li^+$ (0.76 Å), the poor cycle life of metallic K, and safety issues.[192,195] The lower redox potential of $K/K^+$ (−2.93 V for $K/K^+$ compared to −2.71 V for $N_a/Na^+$) *vs.* standard hydrogen electrode (SHE) is responsible for delivering higher working voltages and energy densities in KIBs. Moreover, the weaker acidity leads to a higher conductivity in the electrolyte and a lower interfacial resistance.[192] The introduction of $K^+$ ions to graphitic C materials such as graphite or reduced graphene oxide (RGO) delivers a superior capacity (200 mA h $g^{-1}$) in KIBs compared to SIBs.[196] Numerous studies have incorporated these concepts to enhance the performance of electrodes for KIBs. Prussian blue (PB) is widely used as a cathode material for enhancing the capacity and cycling stability because of its 3D structure.[192,196–198] Ji *et al.* studied the use of magnetic fluoroxalate cathode materials, such as $KFeC_2O_4F$, in KIB applications.[192] $KFeC_2O_4F$ serves as a stable cathode in KIBs and delivers a high discharge capacity of ~112 mA h $g^{-1}$ at 0.2 A $g^{-1}$ with 94% capacity retention after 2000 cycles. Moreover, the battery cell prepared using a $KFeC_2O_4F$ cathode and a soft C anode delivered a high energy density of ~235 W h $kg^{-1}$.[192] An ionic liquid (IL) electrolyte system containing 1-ethyl-3-methylimidazolium chloride/aluminum chloride ($AlCl_3$)-potassium chloride (KCl)-potassium bis(fluorosulfonyl)-imide delivered an excellent ionic conductivity of 13.1 mS $cm^{-1}$ and was non-flammable at room temperature.[195] The battery (3.6 V) prepared using a PB-RGO cathode and a K anode exhibits high power and energy densities of 1350 W $kg^{-1}$ and 381 W $kg^{-1}$, respectively, superior stability over 820 cycles, and a high coulombic efficiency of ~99.9%.

Zhang *et al.* synthesized low-cost K-PB nanoparticles (KPBNPs, $K_{0.220}Fe[Fe(CN)_6]_{0.805}{\cdot}4.01H_2O$) as potential cathode materials for KIBs. The cathode prepared using KPBNPs exhibits a high discharge voltage (3.1–3.4 V) and reversible capacity (73.2 mA h $g^{-1}$) with excellent stability.[196] The full-cell battery set-up constructed using KPBNPs exhibits an excellent capacity of 68.5 mA h $g^{-1}$ at 100 mA $g^{-1}$ with a capacity retention of approximately 93.4% after 50 cycles. The cyclic voltammetry (CV) curve of the KPBNP based electrode indicates the occurrence of a reversible redox reaction at a high potential interval due to the reversible $K^+$ intercalation–deintercalation mechanism involving $C–Fe^{III}–Fe^{II}$.[196] Binder-free cathodes have been developed by combining rusty stainless steel meshes (RSSM) with PB nanocubes and RGO. These cathode materials are highly stable, inexpensive, and exhibit superior electrical conductivity. Use of these cathode materials in KIBs was associated with a high capacity (96.8 mA h $g^{-1}$), rate capability (1000 mA $g^{-1}$, 42% capacity retention), and discharge voltage (3.3 V) along with superior cycle stability (305 cycles, 75.1% capacity retention).[197] Moreover, high-performance cathode materials developed *via* the intercalation of non-flammable electrolytes such as ethylene carbonate (EC) with depotassiated $K_{0.5}MnO_2$ significantly enhance the electrochemical performance of KIBs, delivering a high reversible capacity of 120 mA h $g^{-1}$ and 84% capacity retention after 400 cycles.[199]

Wang *et al.* synthesized molybdenum selenide ($MoSe_2$)–C CSNs having pistachio shuck-like structures by mixing sodium molybdate, oleylamine, and dibenzyl diselenide and degassing at 90 °C for 30 min, followed by two successive pyrolysis steps at 250 °C for 30 min (heating rate: 8 °C $min^{-1}$) and 550 °C for 2 h (heating rate: 8 °C $min^{-1}$) in an inert gas atmosphere.[200] The synthesized unique structures facilitate the diffusion of the $K^+$ ions. Moreover, they maintain their structural stability and exhibit excellent cycle stability during the charge and discharge processes. The electrode fabricated using the ($MoSe_2$)–C material exhibits charge–discharge capacities of 402 and 635 mA h $g^{-1}$ in the first cycle with 63.4% coulombic retention. In addition, it maintains a capacity of 322 mA h $g^{-1}$ at 0.2 A $g^{-1}$ for over 100 cycles and a discharging capacity of 226 mA h $g^{-1}$ at a maximum current density of 1 A $g^{-1}$ after 1000 cycles.[200] According to the results of density functional theory (DFT) studies on ($MoSe_2$)–C CSNs, the accelerated diffusion of $K^+$ ions occurred due to the higher energy barrier of bulk $MoSe_2$ than that of the surface of expanded $MoSe_2$ nanosheets. In addition, the presence of C on the surface facilitates the electron transfer between the CSNs and ensures appreciable structural stability and cycling performance.[200] On the other hand, when the hollow mesoporous C structure obtained by combining MOFs with $CoSe_2$–N-doped C was used as an anode, initial charging–discharging capacities of 448 and 675 mA h $g^{-1}$ were observed along with a coulombic efficiency of 66%, a rate capability of 263 mA h $g^{-1}$ at 2 A $g^{-1}$ and a stable cycle performance of 442 mA h $g^{-1}$ at 0.1 A $g^{-1}$ after 120 cycles.[201] It is plausible that the large volume expansion of the active material caused by pulverization was responsible for its outstanding performance in KIBs.

Chu *et al.* synthesized a bimetallic Fe–Mo selenide-N-doped C (FMSC) based CSN as an active anode for KIBs, which exhibited a high reversible capacity of 298 mA h $g^{-1}$ and maintained a capacity of up to 200 mA h $g^{-1}$ over 100 cycles.[202] The presence of a few layers of bimetallic Se at the core facilitates the transfer of electrons and $K^+$ ions due to the expanded interlayer spacing (0.74 nm) and high intrinsic conductivity. In addition, the presence of a shell layer of flexible N-doped C facilitates the enhanced transfer of electrons and improves the electrocatalytic activity due to the volume expansion of the active materials induced by pulverization. Luo *et al.* prepared PB nanocubes and subjected them to direct sulfurization at 400 °C for 3 h under an Ar atmosphere to synthesize improved $FeS_2$–C nanoparticles.[203] The prepared core–shell nanoparticles exhibit nanocube shapes and deliver an exceptional electrochemical rate capability of 664 mA h $g^{-1}$ at a current density of 0.1 A $g^{-1}$ due to the enhanced electrical conductivity due to volume expansion. Furthermore, the performance of HCSN based

catalysts for different MIBs such as LIBs, SIBs, and KIBs was compared and the results are shown in Table 4.

Table 4 Comparison results of various HCSN based catalysts for different MIBs

| Catalyst | Reversible capacity (mA h $g^{-1}$) | Cycle time | Current density (A $g^{-1}$) | Ref. |
|---|---|---|---|---|
| LIBs | | | | |
| POP-ZIF-8 | 538 | 250 | — | 22 |
| $MC_NC_m$SPs | 578 | 60 | 0.1 | 177 |
| $Co_9S_8$–$MoS_2$–rGO | 2014.5 | 200 | 0.3 | 204 |
| Ge–N-doped graphene | 1220 | 1000 | 1 C | 205 |
| $FeO_x$–N-doped GC | 1071 | 1000 | 1.0 | 206 |
| $MoS_2$ graphene quantum dots | 1031 | 80 | 0.1 | 207 |
| GaP | 305 | 60 | 0.5 | 208 |
| GaP–C | 832 | 100 | 0.5 | 208 |
| $Co_9S_8$–graphene nanocomposites | 754 | 100 | 0.1 | 209 |
| $Sn_4P_3$-graphite | 651 | 100 | 0.1 | 210 |
| $Mn_{1-x}Fe_xP$ | 506 | 40 | 0.1 | 211 |
| $Fe_2P$-GC | 592 | 200 | 0.1 | 212 |
| $Ni_2P$-pGN | 457 | 500 | 0.3 | 213 |
| SIBs | | | | |
| $FeS_2$–$FeSe_2$ | 395 | 270 | 1 | 189 |
| $TiO_{2-x}$-NC | 245.6 | 200 | 0.1 | 191 |
| $Ni_2P$-pGN | 181 | 100 | 0.2 | 213 |
| $NiP_3$ | 980 | 15 | 0.1 | 214 |
| PNAF-NP | 456.34 | 300 | 0.2 | 215 |
| $Sn_4P_3$ | 718 | 100 | 0.1 | 216 |
| $Sn_4P_3$–C | 701 | 50 | 0.1 | 217 |
| CoP-C-RGO-NF | 473 | 100 | 0.1 | 218 |
| $Ni_2P$–C | 433 | 100 | 0.05 | 219 |
| $FeS_2$–C | 551 | 100 | 0.1 | 220 |
| $FeS_2$–C | 330 | 800 | 2.0 | 220 |
| $SnS_2$-NGS | 450 | 100 | 0.2 | 221 |
| $Co_3S_4$-polyaniline | 253 | 100 | 0.2 | 222 |
| FeS-rGO | 547 | 50 | 0.5 | 223 |
| KIBs | | | | |
| $KFeC_2O_4F$ | 112 | 2000 | 0.2 | 192 |
| $Fe_7S_8$-MCC | 336 | 100 | 0.2 | 193 |
| $Fe_7S_8$-MCC | 267 | 500 | 1.0 | 193 |
| KPBNPs | 68.5 | 50 | 0.1 | 196 |
| PB-SSM | 96.8 | 305 | 1 | 197 |
| $K_{0.5}MnO_2$ | 120 | 400 | 0.4 | 199 |
| $MoSe_2$–C | 266 | 1000 | 1 | 200 |
| $CoSe_2$–N-doped C | 442 | 120 | 0.1 | 201 |
| FMSC | 298 | 100 | 0.2 | 202 |
| $FeS_2$-C | 664 | 100 | 0.1 | 203 |
| S,N co-doped thin carbon | 320 | 100 | 0.05 | 224 |
| $Fe_xO$-NFLG-240 | 423 | 100 | 0.05 | 225 |
| Sb-NPMC | 130 | 100 | 1 | 226 |
| $Co_9S_8$-N-C-$MoS_2$ | 100 | 100 | 1 | 227 |
| N-doped porous carbon | 144.4 | 5000 | 1 | 228 |

$Co_9S_8$–$MoS_2$–rGO: cobalt and molybdenum sulphide core–shell nanostructures functionalized with RGO, $FeO_x$-N-doped GC: iron oxide and nitrogen-doped graphitic carbon, GaP: gallium phosphide, GaP-C: pyrolyzed GaP, SnS: tin sulfide, $Sn_4P_3$-graphite: tin phosphide graphite, $Mn_{1-x}Fe_xP$: phosphorus-containing manganese and iron, Ge–N-doped graphene: germanium–nitrogen-doped graphene yolk–shell nanoarchitectures, $Fe_2P$-GC: iron and phosphide doped graphitized carbon, $Ni_2P$-pGN: nickel phosphide on a porous graphene network, PNAF-NP: poriferous nanoflake-assembled flower-like nickel tetraphosphide, CoP-C-RGO-NF: cobalt phosphide with carbon and RGO on nickel foam, $FeS_2$–C: pyrite based carbon, $SnS_2$-NGS: tin sulfide on nitrogen-doped graphene sheets, $MoSe_2$–C: carbonized molybdenum selenide, $Fe_xO$-NFLG-240: iron oxide on N-doped few-layer graphene framework, Sb-NPMC: antimony-nanoparticles encapsulated in nitrogen and phosphorus co-doped mesoporous carbon nanofibers, $Co_9S_8$-N-C-$MoS_2$ DHNCs: N,S doped cobalt and molybdenum carbon.

### 2.3. HCSNs for metal–air-batteries (MABs)

Similar to LIBs, MABs have received considerable attention from the research community. Although LIBs are advantageous for energy storage applications, their construction entails the use of expensive materials. They also suffer from poor recyclability, electrolyte degradation, blockage of cathodic reaction sites by the electrolyte, solid electrolyte interface formation, and large overpotentials.[229,230] In addition, the availability of Li in the earth's crust is limited. MABs are widely used to overcome some of the disadvantages associated with LIBs.[231,232] Many types of MABs have been reported, and they are differentiated based on the metal used to construct the anode. Important examples include Li, Zn, Na, Al, Mg, Fe, and Sn–air batteries. Among the various MABs, Li, Zn, and Na–air batteries have been widely investigated in energy storage applications.

**2.3.1. HCSNs for Li–air batteries (LABs).** LABs, which have been reported to exhibit energy density and overpotential values as high as 3458 W h $kg^{-1}$ and 2.96 V, respectively, are highly important for energy storage applications.[233,234] However, LABs are potentially hazardous since the reactions of Li with water or air can be explosive. Moreover, flammable organic electrolytes are employed in LAB assemblies.[234,235] Other major disadvantages of LABs include the high cost ($\sim$60 USD $lb^{-1}$) of the source materials and extremely high theoretical specific energy density (5400 W h $kg^{-1}$, including oxygen).[234] These issues limit the practical applications of LABs. However, research on improving the electrochemical properties and safety of LABs is ongoing to facilitate their use in energy storage applications. CSNs and HCSNs with controlled surface architectures and morphology are suitable for use as electrode materials in Li–air batteries.[234–238] 3D porous spinel cobaltite core–shell microspheres were synthesized *via* a solvothermal method by mixing nickel nitrate hexahydrate and cobalt nitrate hexahydrate with poly(ethylene glycol)6000 (PEG6000) for 30 min at 80 °C, followed by transfer to a Teflon lined stainless steel autoclave and standing at 200 °C for 10 h. Subsequently, the pre-cleaned and dried sample was calcined at 450 °C for 1 h in the air to form $NiCo_2O_4$ microspheres (Fig. 10(A)).[239] The $NiCo_2O_4$ core–shell microsphere structures obtained at various reaction temperatures are shown in Fig. 10(B)(a)–(d).[239] Uniform-sized microspheres with a diameter of 5 μm were obtained after 3 h of reaction. In the initial stages of the reaction, the microspheres comprised closely packed nanoparticles. However, after 5 h of reaction, nanoflake-like structures were formed (Fig. 10(B)(a)–(d)).[239] The synthetic pathway for preparing the $NiCo_2O_4$ core–shell microspheres utilized in a Li–$O_2$ battery is shown in Fig. 10(B)(e).[239] The obtained microspheres showed excellent electrocatalytic activity and long-term cyclability in Li–$O_2$ cells due to their highly porous structures, high rate capacities, and low overpotentials.[239]

Konderi *et al.* synthesized inexpensive trimolybdenum phosphide ($Mo_3P$) nanoparticles with exceptional bifunctional activities toward the OER and ORR and demonstrated their application in LABs.[240] The fabricated $Mo_3P$ electrode had a long cycle life and a low overpotential and achieved current densities of 7.21 and 6.85 mA $cm^{-2}$ at 2 and 4.2 V, respectively, *vs.* $Li/Li^+$ in the presence of an $O_2$-saturated non-aqueous electrolyte.

Moreover, the catalyst showed low charge and discharge overpotentials of 270 and 80 mV, respectively, with low ORR and OER overpotentials of 4 and 5.1 mV, respectively. The corresponding Tafel slopes were 35 and 38 mV $dec^{-1}$, respectively. MOF-based FeCo alloy cores containing N-doped shell nanoparticles encapsulated in CNTs were prepared *via* pyrolysis at 600 °C. These materials demonstrated superior electrocatalytic performance in LIBs.[241] Exemplary bifunctional catalytic activity was observed in an alkaline electrolyte with a $\Delta E$ ($E_{OER}$@10 mA $cm^{-2}$ − $E_{ORR}$@-1 mA $cm^{-2}$) value of 0.79 V. Moreover, the catalyst exhibited remarkable Li–$O_2$ charge/discharge cycling stability (up to 40 cycles) and retained its catalytic activity after several cycles. The strong chemical/electrical coupling of the FeCo alloy core to the NC shell facilitated electron transfer and protected the alloy from agglomeration or dissolution.[241]

**2.3.2. HCSNs for Zn–air batteries (ZABs).** ZABs have been the subject of intense research owing to their wide applicability in hybrid/electric vehicles and wearable and portable electronic devices.[242,243] The advantages of ZABs over other battery systems include their low cost (depending on the material used in the air electrode), high specific energy density, safety, and environmental friendliness.[242] The ZAB performance is mediated by the air electrode in conjunction with an oxygen electrocatalyst. The air cathode is the most important component of the ZAB which determines the performance and cost of the entire system. The electrocatalysis occurs at a certain point in the three-phase interface constituting the catalyst, electrolyte, and $O_2$. The theoretical specific energy density (1084 W h $kg^{-1}$, including oxygen) of ZABs is considerably lower than that of LIBs. However, the observed values are four times higher than those of current LIBs. In addition, ZABs are more environmentally friendly, safer, inexpensive (~0.9 USD $lb^{-1}$), and have long service lives, low equilibrium potentials, and flat discharge voltages.[244]

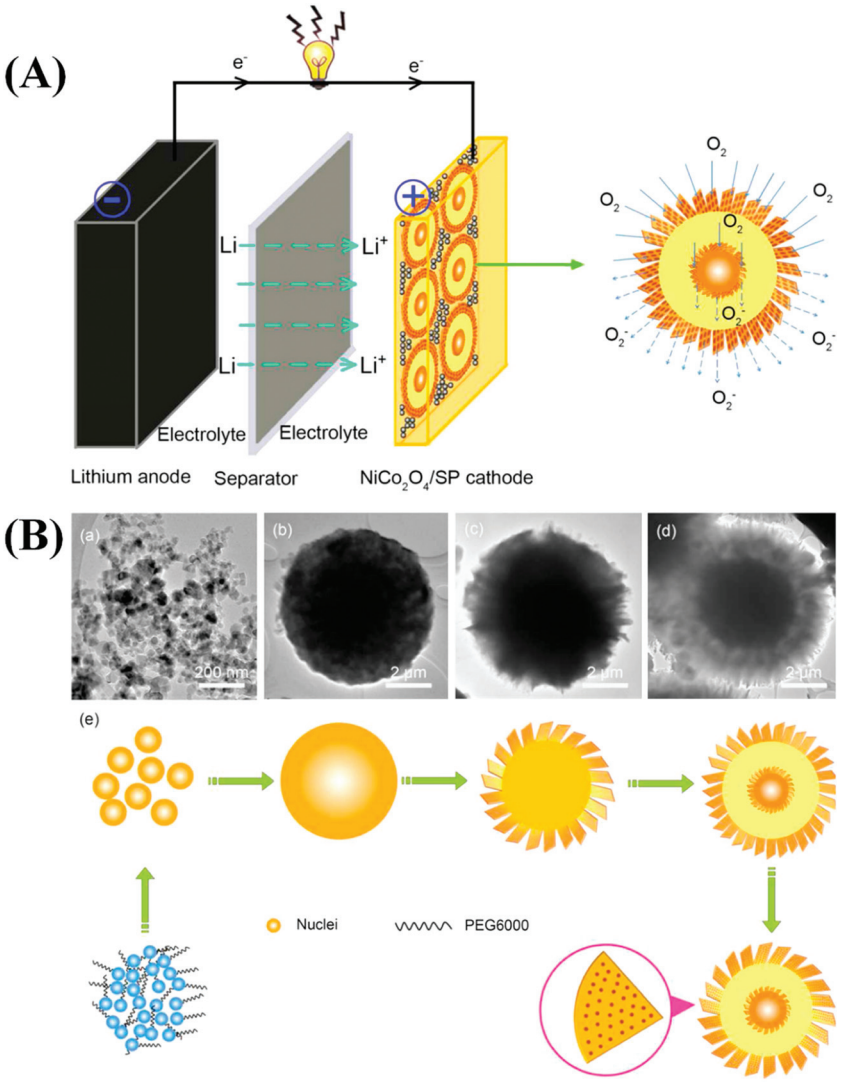


Fig. 10 (A) Representative schematic illustration of the Li–$O_2$ battery catalyzed by 3D porous $NiCo_2O_4$ core–shell microspheres. (B) Time-dependent experiment of $NiCo_2O_4$ at different reaction times: (a) 1 h, (b) 3 h, (c) 5 h, and (d) 10 h, and (e) the corresponding scheme of the reaction process. Reproduced from ref. 239 with permission from Elsevier Ltd.

These properties indicate the viability of the industrial production of ZABs. A suitable combination of an oxygen electrocatalyst layer, a GDL, and an air electrode determines the performance and cost of a ZAB.

To date, a diverse range of electrocatalysts with superior ORR and OER activities have been developed using perovskite oxides, heteroatom-doped C, and transition metal nitrides/oxides/sulfides, which are applicable in ZABs.[242–245] HCSNs with bifunctional properties have been extensively used in ZABs.[246–258] An MCO/CNF@NC catalyst has demonstrated outstanding catalytic performance in ZABs with a discharge capacity of 478 F $g^{-1}$ at a discharge current density of 1 A $g^{-1}$.[259] The OER activity of the catalyst was associated with a low overpotential (0.41 V) at a current density of 10 mA $cm^{-2}$ and matching onset (1 V *vs.* RHE) and half-wave potential (0.76 V *vs.* RHE) values were obtained with an ORR activity that was approximately 40 mV lower than that of a Pt–C catalyst. The catalyst also exhibited a lower ORR/OER potential gap (0.88 V), which indicated the excellent bifunctional behavior of the catalyst. Furthermore, the specific capacitance and energy density values of the synthesized catalyst were determined to be 695 mA h $g^{-1}_{zn}$ and 778 W h $kg^{-1}_{zn}$, respectively, at 20 mA $cm^{-2}$.

Chen *et al.* synthesized an N-doped C material containing Fe-enriched $FeNi_3$ intermetallic nanoparticles by plasma engineering using a maximum amount of iron(II) chloride tetrahydrate and adjustable amounts of nickel(II) acetate tetrahydrate in the presence of pyridine, and the obtained material was further pyrolyzed at 800 °C for 1 h under an $N_2$ atmosphere (1.5 cc $min^{-1}$).[260] The synthesized Fe-enriched $FeNi_3$/NC electrocatalyst had excellent bifunctional catalytic activities toward the ORR and OER. The schematic of the reaction pathway of the corresponding ZAB is shown in Fig. 11(a).[260] The open circuit

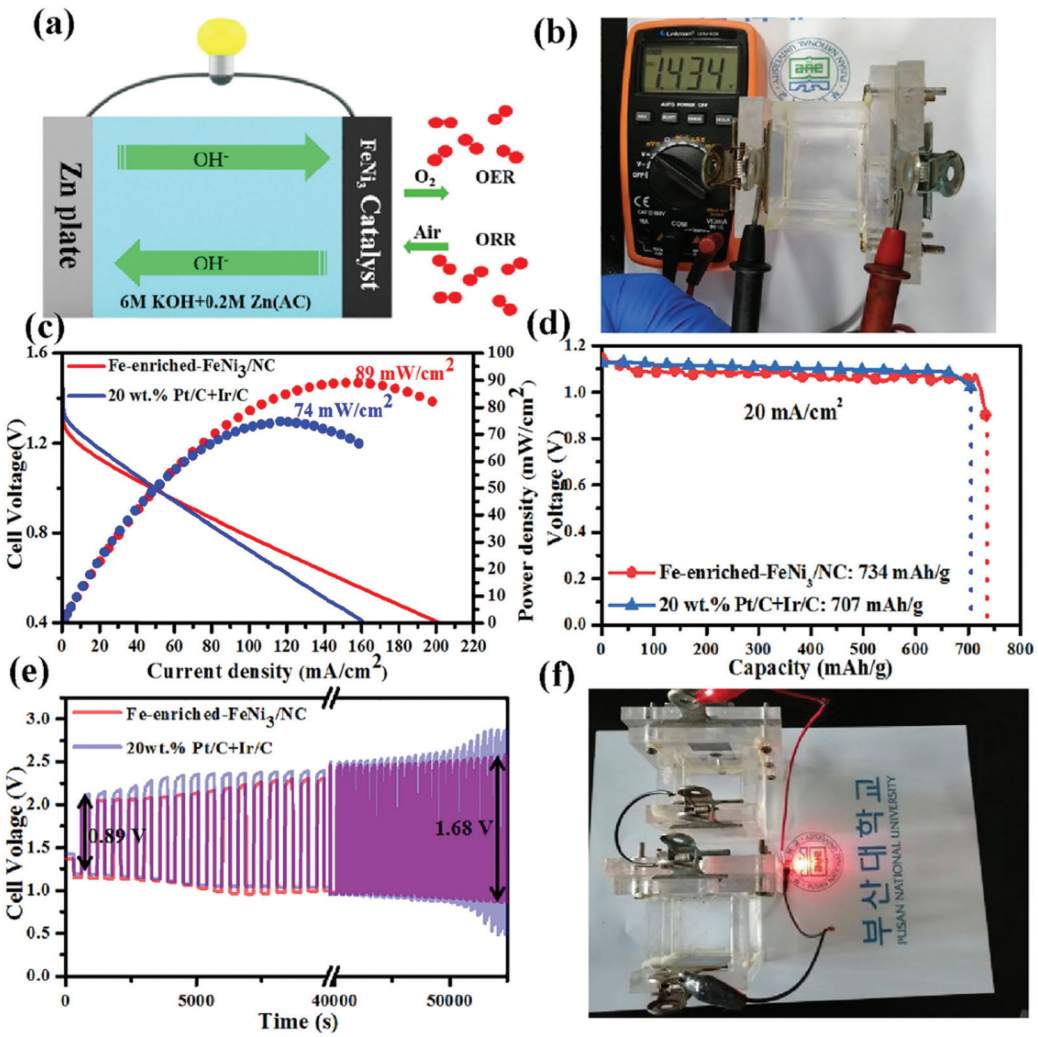


Fig. 11 (a) A schematic illustration of the home-made Zn–air battery. (b) OCV of the as-assembled Zn–air battery with an Fe-enriched-$FeNi_3$/NC air–cathode. (c) The discharge polarization curves and the corresponding power density curves of the battery with Fe-enriched-$FeNi_3$/NC and 20 wt% Pt/C + Ir/C air-electrodes, respectively. (d) Specific capacity plots of Fe-enriched-$FeNi_3$/NC and 20 wt% Pt/C + Ir/C based Zn–air batteries tested at 20 mA $cm^{-2}$. (e) Galvanostatic discharge–charge cycling curves of Fe-enriched-$FeNi_3$/NC and 20 wt% Pt/C + Ir/C based batteries at a current density of 10 mA $cm^{-2}$, respectively. (f) Photograph of a red LED lightened by two series-connected liquid Zn–air batteries with an Fe-rich-$FeNi_3$/NC air–cathode. Reproduced from ref. 260 with permission from Elsevier Inc.

potential of the Fe-enriched $FeNi_3$/NC electrocatalyst was 1.43 V (Fig. 11(b)).[260] In addition, the synthesized material delivered a low charge/discharge voltage gap (0.89 V) with a peak power density, current density, and specific capacity of 89 mW $cm^{-2}$, 200 mA $cm^{-2}$, and 734 mA h $g^{-1}$, respectively, for 1 mg $cm^{-2}$ of catalyst loading. The corresponding ZAB exhibited appreciable stability, cycle durability, and rechargeability (Fig. 11(c)–(e)).[260] On the other hand, the corresponding values for the electrode prepared using 20 wt% Pt–C and Ir–C were 74 mW $cm^{-2}$, 160 mA $cm^{-2}$, and 707 mA h $g^{-1}$, respectively. When the Fe-enriched $FeNi_3$–NC electrocatalyst was utilized for optical imaging by connecting a red light-emitting diode (LED) to two liquid ZABs (in series), continuous illumination was observed for over 10 days (Fig. 11(f)).[260]

A Co@CNT based CSN bifunctional electrocatalyst obtained from ZIF-67 and melamine *via* a simple surface treatment demonstrated exceptional stability, low charge/discharge voltage gap, and larger power density in ZABs.[257] Fig. 12(a) shows a schematic illustration of the synthesis of Co@CNT from ZIF-67.[257] ZIF-67 was modified by mixing with melamine which acted as a carbon and nitrogen source. The sample was subsequently pyrolyzed at 700 °C for 3 h under an $N_2$ gas flow at a rate of 2 °C $min^{-1}$. The electrode fabricated from the synthesized Co@CNT CSNs delivered a superior bifunctional ORR and OER electrocatalytic activity (Fig. 12(a)).[257] DFT studies were conducted to predict the free energy of the bifunctional electrocatalyst in an alkaline (pH = 13) solution and a probable mechanism was investigated (Fig. 12(b)).[257] The ORR catalytic reaction mediated by Co@CNT occurred *via* four-electron transfer pathways with the adsorption of three active species (OOH*, OH*, and O*) on the catalytic surface. The Gibbs free energies ($\Delta G$ values) corresponding to the adsorption of OOH*, OH*, and O* were −0.44, −0.56, and −0.41 eV, respectively, while that corresponding to the desorption of OH* was −0.41 eV. The highest $\Delta G$ value observed corresponded to the adsorption of OH*, which indicated that the adsorption of OH* constituted the rate-determining step (RDS) of the catalyst. In addition, the low overpotential value of 0.56 eV indicates the excellent ORR performance of the catalyst. The ORR catalytic behavior of the catalyst was investigated in alkaline and acidic environments using 0.1 M KOH and 0.5 M $H_2SO_4$, respectively, and the obtained results were correlated with K–L plots acquired at different rotating speeds of the catalyst electrodes in the respective electrolytes (Fig. 12(c)–(h)).[257] The Co–CNT electrocatalyst exhibited appreciable ORR stability and OER performance with a low overpotential and high catalytic activity. These results demonstrate the potential utility of the bifunctional catalyst in ZABs. Here, Zn foil acts as the anode and the Co–CNT catalyst (0.5 mg $cm^{-2}$) loaded on carbon cloth (CC)-GDL acts as the cathode, while zinc chloride ($ZnCl_2$, 0.2 M) containing 6 M KOH behaves as the electrolyte. The Co–CNT (1:1) catalyst delivers superior battery performance at a high current density with a reduced charge/discharge voltage gap (a current density of 50 mA $cm^{-2}$ necessitated a voltage gap as low as 1 V) compared

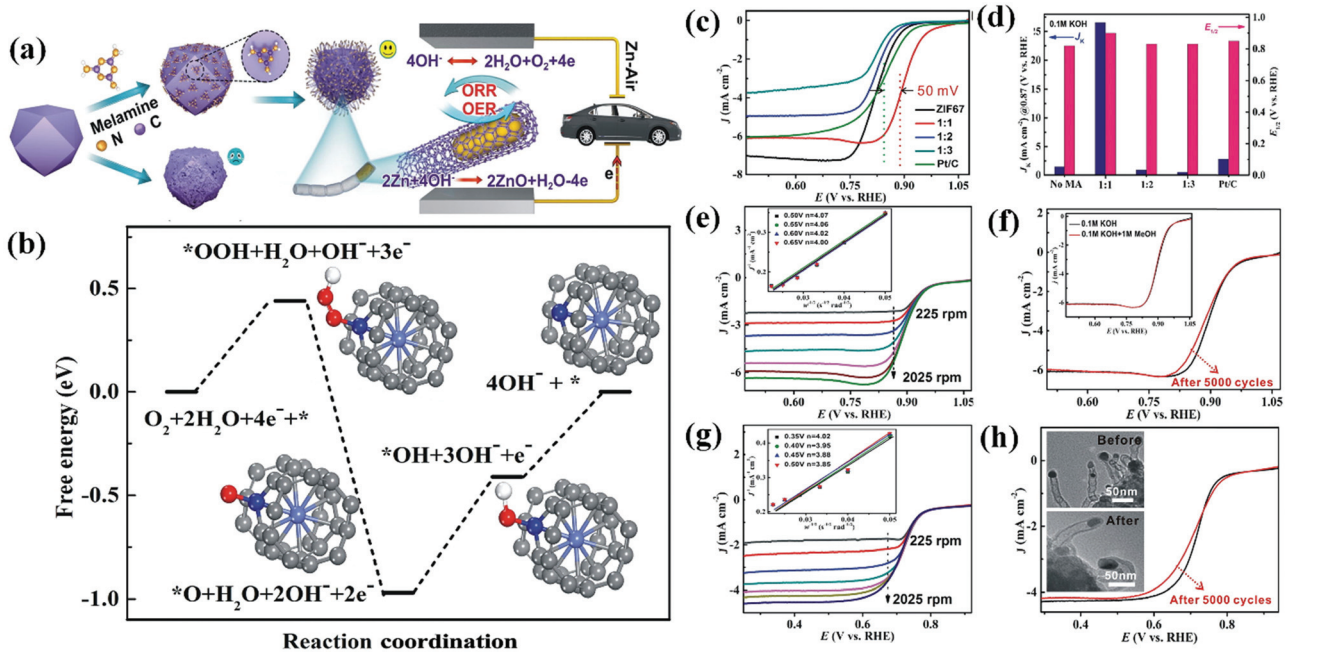


Fig. 12 (a) Schematic illustration of the synthetic strategy for Co@CNTs. (b) Free-energy diagram for the ORR on Co@CNTs in alkaline (pH = 13) media. ORR activities of Co@CNTs in both alkaline and acidic media. (c) LSV curves and (d) $J_K$ and $E_{1/2}$ of Co@CNTs and other comparative catalysts in 0.1 M KOH. (e) LSV curves of the Co@CNTs at different rotating rates. Inset : the K–L plot at various potentials. (f) LSV curves of Co@CNTs and the sample after 5000 cycles (the inset shows 0.1 M KOH solution with and without 1 M methanol). (g) LSV curves of Co@CNTs at different rotating rates in 0.5 M $H_2SO_4$. Inset: the K–L plot at various potentials. (h) LSV curves of Co@CNTs and the sample after 5000 cycles (inset: TEM images before and after 5000 cycles). MA : melamine; 1 : 1, 1 : 2 and 1 : 3 are the ratios of $weight_{ZIF-67}$ : $weight_{melamine}$, respectively. Reproduced from ref. 257 with permission from Science Press and Dalian Institute of Chemical Physics, Chinese Academy of Sciences. Published by Elsevier B.V. and Science Press.

with that observed in the case of the Pt–C + Ir–C catalyst. Additionally, Co–CNT (1:1) delivered a peak power density of 149.2 mW $cm^{-2}$ which was higher than that offered by the Pt–C–Ir–C catalyst (90 mW $cm^{-2}$). These results demonstrate the outstanding rechargeability and reactivity of the Co–CNT (1:1) catalyst.[257] According to the galvanostatic charge/discharge cycling curve of the Co–CNT (1:1) catalyst determined at 2 mA $cm^{-2}$, a discharge voltage as high as 1.2 V was observed with a modest charge voltage of 2 V, which corresponded to a charge–discharge gap of 0.8 V and an energy efficiency of over 60%. These results, which were maintained for over 40 h (120 cycles), indicated the superior stability of the catalyst due to its efficient electronic conductivity, controlled surface texture with a high surface area, interfacial physicochemical properties, and high intrinsic activity.[257] Zhao *et al.* developed a B and N heteroatom doped ultrathin carbon nanosheet *via* a simple and effective sodium chloride (NaCl)-assisted pyrolysis method.[261] The BN–C produced is made up of ultrathin nanosheets as thin as 5 nm and has a large surface area of 1085 $m^2$ $g^{-1}$ with both micro- and mesopores. BN–C has strong ORR activity, with a half-wave potential of 0.8 V. Furthermore, in comparison to the commercial Pt–C + $RuO_2$ based battery, the BN–C + $RuO_2$ based Zn–air battery with a liquid electrolyte demonstrates improved performance and cycle stability after 1000 continuous discharge–charge cycles (for 14 days of operation).[261] The specific capacity of the BN–C + $RuO_2$ catalyst is determined to be 802 W h $kg_{Zn}^{-1}$ at 5 mA $cm^{-2}$, which is higher than the capacity of the Pt/C + $RuO_2$ based Zn–air battery, which was only 774 W h $kg_{Zn}^{-1}$ based on the amount of Zn that was consumed.[261] The author has generated atomically distributed Co sites that are anchored on interconnecting B,N-doped carbon nanotubes (B, N, Co–C nanotubes).[262] These nanotubes are prepared using a simple molten-salt-assisted pyrolysis of B–N–Co precursors which comes after chemical etching. Various other HCSN based materials have demonstrated efficient catalytic activity in ZABs. We also compared and summarized the results of some of the HCSN catalysts used in ZIBs (Table 5).

An *et al.* used DFT simulations to assess the surface energetics of $NiFe_2O_4$ and $FeNi_2S_4$ clusters connected *via* their (311) or (100) planes and projected the link between the interface and catalysis of these clusters for ZIBs (Fig. 13).[281] The increased electrical affinity of oxygen causes the electron to move from the $FeNi_2S_4$ domain to the $NiFe_2O_4$ domain, according to DFT investigations, which also demonstrate that oxygen prefers to adsorb on surface Ni near the interface. These also suggest that $NiFe_2O_4$ and $FeNi_2S_4$ domains have a significant electrical connection. The results of their calculations showed that the intermediates *O, *OH, and *OOH scaled linearly, allowing the use of oxygen adsorption energy ($E_0$) as an universal descriptor to forecast and assess the ORR and OER activities.[281] It is well known that metal oxide catalysts experience excessively high oxygen adsorption, which slows down the reaction kinetics. Therefore, improving the oxygen electrocatalytic characteristics of the catalysts requires significantly reduced $E_0$ at the $NiFe_2O_4$/

Table 5 Comparison of the performance of ZIBs with various HCSN based catalysts

| Catalyst | Specific capacity (mA h $g_{zn}^{-1}$)@ j (mA $cm^{-2}$) | Energy density (Wh $kg_{zn}$ $g^{-1}$)@j (mA $cm^{-2}$) | Power density (mW $cm^{-2}$) | Current density (mA $cm^{-2}$) | Ref. |
|---|---|---|---|---|---|
| CMT–CNT | 781.7@10 | 930.2@10 | 160.6 | 10 | 255 |
| $Co_4N$-CNW-CC | 774@10 | — | 174 | 10 | 263 |
| Co-SAs-NC | 897.1@20 | — | 105 | 20 | 264 |
| N-GCNT-FeCo-3 | 872.2@100 | 653.2@100 | 89.3 | 100 | 265 |
| CoNi-NHCS-TUC-3 | 756.5 | 957 | 255.9 | 361.8 | 266 |
| GNCNTs-4 | 728 | — | 253 | 383 | 267 |
| ZOMC | 795.3@5 | 969.4@5 | 221.1 | 5 | 268 |
| ZOMC | 697.9@10 | 772@10 | 221.1 | 10 | 268 |
| CoNi-BCF | 710.9@10 | 853.1@10 | 155.1 | 10 | 269 |
| NDGs-800 | 750.8@10 | 872.3 | 115.2 | 10 | 270 |
| FeNC–S–$Fe_xC$–Fe | 663@10 | 795@10 | 149.4 | 10 | 271 |
| FeS–$Fe_3C$-NS-C-900 | 750 | — | 90.9 | 20 | 272 |
| NCN-1000-5 | 672@10 | 805@10 | 207 | 10 | 273 |
| NPCS-900 | 625@20 | 656.25@20 | 79 | 20 | 274 |
| SCoNC | 690@5 | 945@5 | 194 | 5 | 275 |
| CoZn-NC-700 | 578@10 | 694@10 | 152 | 10 | 276 |
| $NiCo_2S_4$-g$C_3N_4$-CNT | 485.7@10 | 530.5@10 | 142 | 10 | 277 |
| Zinc plate-Pt–SCFP-CC | 790.4@5 | — | 122 | 10 | 278 |
| Zinc plate-Co–$Co_3O_4$-NAC-NF | 721@10 | — | 164 | 10 | 279 |
| Fe–$Co_4N$–N–C | 806@5 | 934 | 105 | 5 | 280 |

CMT–CNT: carbon microtube@nanotube core–shell, $Co_4N$-CNW-CC: metallic $Co_4N$ with carbon fiber network on carbon cloth, Co-SAs-NC: Co single atoms on N-doped carbon, N-GCNT-FeCo-3: bimetal FeCo nanoparticles enveloped by N-doped graphitic carbon nanotubes, CoNi-NHCS-TUC-3: cobalt–nickel supported on nitrogen-doped hollow spherical carbon and tubular carbon, GNCNTs-4: nitrogen-doped carbon nanotubes-graphene, ZOMC: pyrolysis of ZIF-67 to form ordered macroporous carbon, CoNi-BCF: CoNi alloy nanoparticles supported by a butterfly wing-derived carbon framework, NDGs-800: pyridinic-N-dominated doped defective graphene, FeNC–S–$Fe_xC$–Fe: sulfuration of an Fe–N–C catalyst containing $Fe_xC$–Fe species, FeS–$Fe_3C$-NS-C-900: FeS–$Fe_3C$ nanoparticles embedded in a porous N,S-dual doped carbon, NCN-1000-5: nitrogen doped ultrathin carbon nanosheets, NPCS-900: nitrogen and phosphorous co-doped carbon spheres, SCoNC: monodisperse Co single atoms on a nitrogen-doped 2D carbon nanosheet, CoZn-NC-700: bimetallic nitrogen-doped carbon, $NiCo_2S_4$-g$C_3N_4$-CNT: $NiCo_2S_4$-graphitic carbon nitride/carbon nanotube, zinc plate-Pt–SCFP-CC: platinum with a perovskite on carbon cloth, zinc plate-Co–$Co_3O_4$-NAC-NF: Co single-atom anchored on $Co_3O_4$ and nitrogen-doped active carbon on nickel foam, Fe–$Co_4N$–N–C: co-doped Fe–$Co_4N$–N–C nanosheet array.

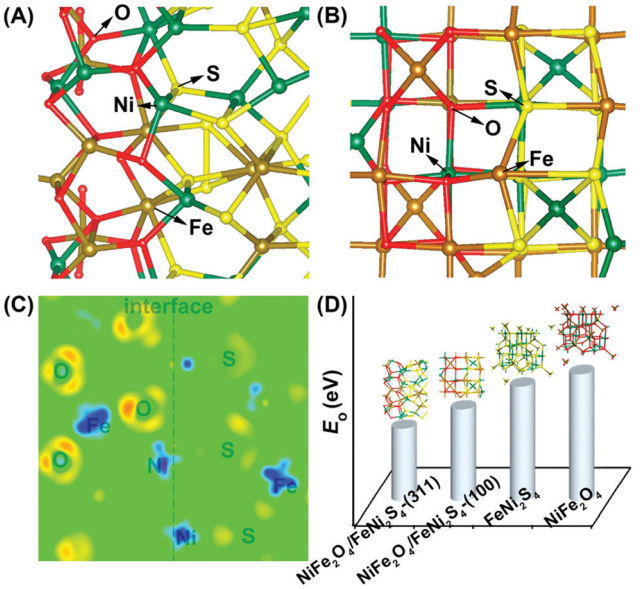


Fig. 13 (A), (B) Optimized geometry of oxygen adsorption over the $NiFe_2O_4/FeNi_2S_4$(311) interface model (A) and the $NiFe_2O_4/FeNi_2S_4$(100) interface model (B). (C) Differential charge density of the cross-sectional view of the $NiFe_2O_4/FeNi_2S_4$(311) interface model. The red/light (blue/dark) areas mark an increase (decrease) of the electron density. (D) Computational surface EO comparison of $NiFe_2O_4/FeNi_2S_4$-(311), $NiFe_2O_4/FeNi_2S_4$-(100), $FeNi_2S_4$, and $NiFe_2O_4$. Reproduced from ref. 281 with permission from the American Chemical Society.

$FeNi_2S_4$ interface.[281] Wang *et al.* also proposed the mechanism of vertically-aligned porous nanoarrays made of ultrafine nitrogen-doped cobalt oxide (NP-$Co_3O_4$) nanoparticles (4–5 nm) prepared *in situ* on carbon cloth (CC) by mildly oxidizing Co-based zeolitic-imidazolate-framework (Co-ZIF) nanoarrays (Fig. 14).[282]

**2.3.3. HCSNs for sodium–air batteries (SABs).** SABs have certain distinct advantages that enable their successful utilization in energy storage applications. Notably, they have a high theoretical energy density (1084 W h $kg^{-1}$) and high specific capacitance, and are environmentally friendly. In addition, Na is inexpensive compared with other metals due to its abundance.[181,283,284] Therefore, SABs are a viable alternative to Li–air and other MABs.[284,285] However, SABs suffer from poor cycling stability, high overpotential, and low energy efficiency owing to the sluggish ORR/OER kinetics of the air electrode.[283,286] In addition, the presence of binders, such as Nafion, polyvinylpyrrolidone (PVP), and polytetrafluoroethylene (PTFE), restrict electron/ion transfer, which diminishes the performance and electrical conductivity.[283,286,287] SABs and K–air batteries also suffer from the formation of stable superoxides as the final discharge product.[287] These disadvantages are overcome by preparing ORR/OER bifunctional electrocatalysts in the absence of binders using judiciously chosen materials to synthesize Na-superoxides by solution-mediated routes to reduce the formation of superoxides.[283,286–288] In this section, we discuss the improvements achieved in the performance of SABs using HCSNs. A typical bifunctional electrocatalyst has been produced by depositing Pt–Ni nanoparticles on NiFe layered double hydroxide (LDH) nanosheets in the presence of a binder-free Ni foam substrate, which exhibits excellent ORR–OER activity in SABs with a low initial overpotential (0.5 V), high charge–discharge (round trip) efficiency (~79.9%), and outstanding stability and rechargeability for over 300 cycles without losing its structural integrity.[283] Cheon *et al.* designed highly graphitic nanoshells encapsulated in mesoporous C (GNS-MC) which exhibited efficient bifunctional oxygen electrocatalytic properties, including high activity, long-term stability, and durability toward the ORR/OER. It is one of the most important

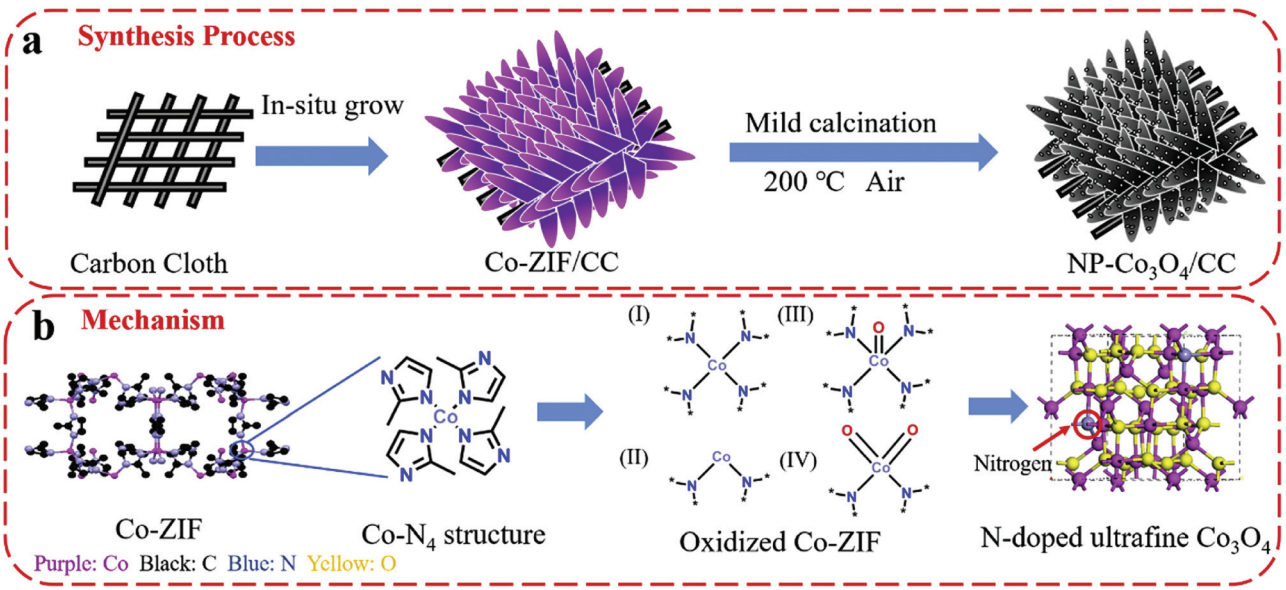


Fig. 14 Schematic demonstration of (a) the fabrication process of NP-$Co_3O_4$/CC and (b) the proposed mechanism of nitrogen doping in cobalt oxide lattices. Reproduced from ref. 282 with permission from Elsevier B.V.

reports on aqueous SABs.[289] Here, Na metal and a catalyst-coated C paper were used as the anode and cathode, respectively, while 0.1 M sodium hydroxide (NaOH) and 1 M sodium trifluoromethanesulfonate ($NaCF_3SO_3$)–tetraethylene glycol dimethyl ether (TEGDME) were used as aqueous and non-aqueous electrolytes, respectively, for the cathode and anode. Furthermore, Na superionic conductor (NASICON) was used as a solid electrolyte to enable the careful transfer of Na ions from the cathode to the anode, while preventing direct contact between the aqueous and non-aqueous electrolytes. The electrochemical reactions at the anode and cathode occurred according to eqn (4)–(6):[289]

$$\text{Anode: } Na \leftrightarrow Na^+ + e^- \quad E^\circ = +2.71\ V \tag{4}$$

$$\text{Cathode: } O_2 + 2H_2O + 4e^- \leftrightarrow 4OH^- \quad E^\circ = +0.40\ V \tag{5}$$

$$\text{Overall: } 4Na + O_2 + 2H_2O \leftrightarrow 4NaOH \quad E^\circ = 3.11\ V \tag{6}$$

The charge–discharge behavior of the GNS-MC catalyst in an aqueous SAB was characterized by a lower $\Delta V$ ($\Delta V$ denotes the voltage differences between charge and discharge voltages) (115 mV) compared with the values observed for the Pt–C (179 mV), Ir–C (364 mV), and C paper (698 mV) catalysts, which was indicative of the outstanding performance of the catalyst. The charge–discharge cycle stability of the GNS-MC electrocatalyst was examined for 10 cycles, and the results indicated that the electrocatalytic properties of the material were sustained.[289] Recent research has focused on improving the performance of the electrocatalysts used in SABs.[290–293] The reported results demonstrate the outstanding activity of the electrocatalysts used in SABs and establish the excellent utility of SABs in ECS applications.[294,295]

### 2.4. HCSNs for Li–sulfur batteries (LSBs)

Similar to the metal-ion and metal–air batteries discussed in previous sections, LSBs have attracted considerable attention from the research community.[296] LSBs are noted for being cost-effective and demonstrating enhanced gravimetric energy density and safety.[297–301] The theoretical energy density of Li–S rechargeable batteries can be as high as 2600 W h $kg^{-1}$, which makes them highly suitable for application in various energy storage systems.[299,302] S is highly inexpensive compared to transition metals (*e.g.*, Co and Mn) and phosphates, which are used to develop Li-based batteries.[297] Moreover, the synthesis of LSB electrode materials is considerably easier and safer compared to those of Li-ion and Li–air battery electrode materials. Therefore, S can be widely used to develop rechargeable batteries with high energy densities.[297,303] However, LSBs suffer from the incomplete utilization of S due to the insulating nature and low conductivity of S. The instability of the Li metal surface is another disadvantage. The electrode material experiences a considerable volumetric expansion of ~80% during lithiation which involves pulverization of the active material. These factors result in decreased coulombic efficiency and capacity decay, sluggish redox kinetics, and shuttle effects.[297,299] These disadvantages can be addressed by the incorporation of various functional materials in the S cathodes, such as metal compounds, porous carbon, graphene, RGO, and CNTs.[297] Enhanced accumulation of S can be achieved in LSBs using a C support. The presence of a C support improves S loading and results in a high surface area and large pore volume. The formation of hierarchical meso–microporous structures with robust mechanical properties is also observed. C supported S delivers superior electrochemical performance due to its improved conductivity.[302] Gai *et al.* recently built a high performance LSB using multifunctional 3D-mesoporous carbon nanocomposites such as RGO with embedded Co nanoparticles and elemental N (Co–NrGO) followed by ground mixture with powdered S at a mass ratio of 1 : 6 (Co–NrGO–S) used as cathode-separator-coated interlayers and working electrodes in assembled Li–S cells, respectively.[296] The LSB cells that were developed exhibited outstanding endurance (905 mA h $g^{-1}$ in the 250th cycle at 0.5 or 0.2 C), high-rate capabilities (835 mA h $g^{-1}$, 2.0 C), and superior cycling stability (1070 mA h $g^{-1}$ in the 100th cycle at 0.2 C). These results also further proved that the lack of Co–NrGO coatings and/or Co nanoparticles in the constructed LSB may be insufficient to ensure enhanced S availability which leads to a poorer performance in the LSB. However, the better performance of Co–NrGO–S is mostly due to the catalytic capacity of the inserted metallic Co nanoparticles for the reversible transformation of $S_8$ into $Li_2S$.[296]

Zhen *et al.* prepared S-doped ordered meso@microporous core–shell (S/MMCS) C nanoparticles and compared their electrochemical performance with those of S doped mesoporous C (S/mesoC) and S doped microporous C (S/microC) materials in LSBs.[302] The cores of the developed structures facilitate increased S loading due to their ordered porous structures with high surface areas and pore volumes, whereas the shells having microporous C structures accommodate lower amounts of S. The overall loading of S in the meso–microporous structure is thus optimized (Fig. 15(A)).[302] The prepared S/mesoC, S/microC, and S/MMCS electrodes exhibit excellent specific capacities of 1123 (739), 1071 (322), and 1212 (734), respectively, after 2 charge/discharge cycles (Fig. 15(B)(a) and (b)).[302] The S/MMCS electrodes exhibit appreciable capacity retention, which is evidenced by the capacity values of 1014 (615) and 837 (506) mA h $g^{-1}$ observed after 100 and 200 cycles, respectively. They also exhibit a high current density of 0.5 C (here C refers to the capacity of a battery), capacity retention exceeding 80%, and 95% coulombic efficiency (Fig. 15(c)).[302] The LSB cell prepared using S/MMCS exhibits discharge capacities of 1182 (715), 1038 (628), 930 (563), 840 (508), and 605 (366) mA h $g^{-1}$ at 0.1, 0.2, 0.5, 1, and 2 C, respectively (Fig. 15B(d)).[302] According to these results, the superior electrical conductivity, large pore volume, and high S loading of S-MMCS ensure its utility in LSBs. Similarly, various S-doped C-containing CSNs were synthesized by various techniques and applied successfully in LSBs.[304–307] Two dimensional S (5 mg $cm^{-2}$)-doped C yolk–shell nanosheets were prepared, which displayed volumetric and areal capacitance values of 1330 mA h $cm^{-3}$ and 5.7 mA h $cm^{-2}$, respectively. The areal capacitance was enhanced (up to 11.4 mA h $cm^{-2}$) upon increasing the S doping from 5 to 10 mg $cm^{-2}$.[304] Tao *et al.* synthesized an efficient anode material for Li–Na-ion batteries using multi-heteroatom (N, P, and S) decorated C containing magnetite-based iron oxide

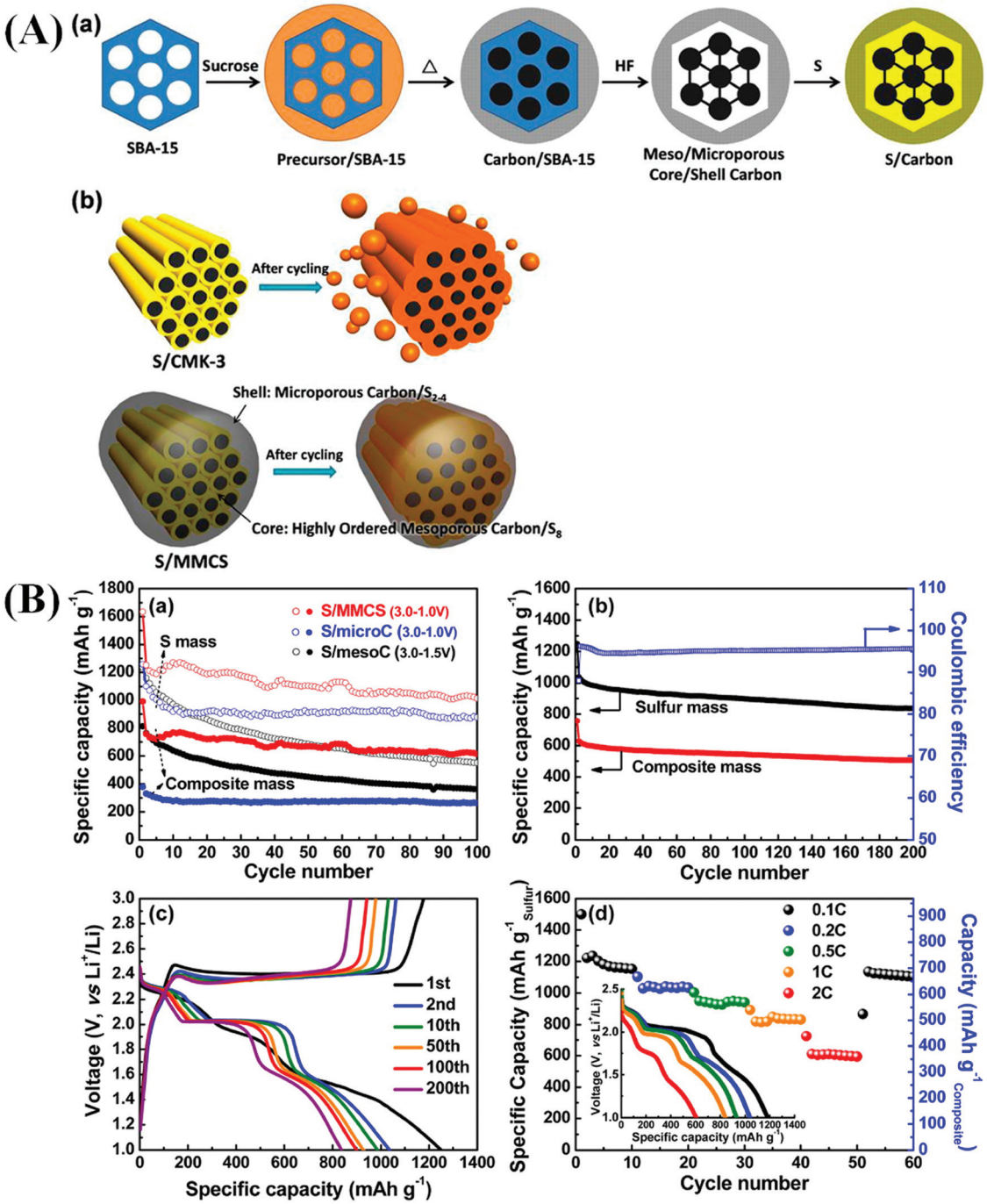


Fig. 15 (A) Schematic of preparation of the highly ordered meso–microporous core–shell (MMCS) carbon and sulfur/carbon composite (a). Schematic of the mesoC/S8-microC/S2–4 core–shell structure (b). (B) Cycle performances of S/MMCS, S/mesoC, and S/microC at 0.1C (a and b), voltage profiles during cycling at 0.5C (c), and rate capacities at various C-rates of S/MMCS in the voltage range of 3.0–1.0 V *vs.* $Li^+$/Li (d). The inset of (d) shows the discharge voltage profiles at current densities from 0.1 to 2C. Reproduced from ref. 302 with permission from the American Chemical Society.

($Fe_3O_4$) nanospheres which exhibited excellent electrochemical performance, as evidenced by the high specific capacity and cycle stability.[305] $Fe_3O_4$@doped C@graphene ($Fe_3O_4$@C@G) 3D structured anode materials were synthesized, which delivered a reversible capacity of 919 mA h $g^{-1}$ at 0.1 A $g^{-1}$ in LIBs. The corresponding value observed for an S-ion battery was 180 mA h $g^{-1}$ at 0.1 A $g^{-1}$ after 600 cycles.[305]

## 3. Conclusions

In this review, we have briefly described the various properties of HCSNs and the recent advances made in their applications to fuel cell and battery technologies. The fuel cell activity of HCSNs has been improved by optimizing the synthetic processes and adopting different approaches, such as the insertion

of dissimilar metals in the HCSN cores, formation of alloys with unassociated metals, controlling the size, shape (or facet), and morphology, and application of sacrificial materials as supports.[54,308] The main advantage of CSNs is the tunability of their core and shell compositions. Tuning is performed by incorporating one or more low-cost transition metals or metal oxides either in the core or in the shell to reduce the proportion of Pt, which significantly improves the catalytic activity and tolerance against different environments. Some of the important challenges encountered during the application of CSNs in fuel cells include insufficient catalytic stability, unoptimized catalyst designs, and insufficient understanding of ORR activity and mechanisms.[54]

The catalytic activity of CSNs in fuel cells is enhanced by doping them with heteroatoms, which increases the number of active sites and defects while modifying the facets of the nanoparticles on the shell. Rigorous studies are necessary on the structural modifications of the materials induced by catalytic applications along with theoretical modeling and experimental measurements. In addition, optimization of the MEA fabrication process is required by the respective catalyst inks/layers and the associated testing parameters.[54] The use of Pt in electrode fabrication should be minimized to reduce costs and enhance the stability and tolerance against the external environment. Earth-abundant elements can be successfully used to reduce the proportion of Pt in the CSN cores.[309] However, the 3d transition metals used in CSN cores suffer from electrochemical corrosion. This disadvantage can be addressed by using carbides, nitrides, and oxides to construct the cores of CSNs featuring noble metal shells.[309]

Bifunctional ORR/OER catalysts have excellent electrochemical properties, which make them highly useful for various types of battery applications. The performances of bifunctional electrocatalysts are improved by controlling the crystal facets, defects, morphologies, and phases through strain engineering and the introduction of heteroatoms and the formation of M–N–C structures. Highly active electrocatalysts for fuel cells and Li-ion–air–S batteries are developed by doping C nanomaterials with heteroatoms. Research aimed at the continuous improvement of performance and stability, and reduction of the final cost of the electrocatalysts is highly important for addressing the future energy demands. More studies are necessary to develop improved catalysts for use in fuel cell and battery applications.

## Author contributions

S. N. contributed to the conceptualization, writing the original draft, and review and editing. M. D. and N. P. contributed to the literature review, methodology, and summary. K. P. contributed to the outline of the review article as well as review and editing. K. H. P. contributed to the conceptualization, supervision, review and editing, and funding acquisition. All the authors discussed and revised the manuscript.

## Conflicts of interest

There are no conflicts to declare.

## Acknowledgements

This research was supported by the Basic Science Research Program through the National Research Foundation of Korea (NRF) grant funded by the Korea Government (MSIP) (NRF-2020R1I1A3067208).

## Notes and references

1 S. Nagappan, M. Duraivel, S. A. Hira, K. Prabakar, C.-S. Ha, S. H. Joo, K. M. Nam and K. H. Park, *J. Mater. Chem. A*, 2022, **10**, 987–1021.
2 S. W. Kim, J. Ryu, C. B. Park and K. Kang, *Chem. Commun.*, 2010, **46**, 7409–7411.
3 E. Lim, J. Changshin, M. S. Kim, M. H. Kim, J. Chun, H. Kim, J. Park, K. C. Roh, K. Kang, S. Yoon and J. Lee, *Adv. Funct. Mater.*, 2016, **26**, 3711–3719.
4 H. P. Feng, L. Tang, G. M. Zeng, J. Tang, Y. C. Deng, M. Yan, Y. N. Liu, Y. Y. Zhou, X. Y. Ren and S. Chen, *J. Mater. Chem. A*, 2018, **6**, 7310–7337.
5 P. Strasser, S. Koh, T. Anniyev, J. Greeley, K. More, C. Yu, Z. Liu, S. Kaya, D. Nordlund, H. Ogasawara, M. F. Toney and A. Nilsson, *Nat. Chem.*, 2010, **2**, 454–460.
6 A. M. El-Toni, M. A. Habila, J. P. Labis, Z. A. Alothman, M. Alhoshan, A. A. Elzatahry and F. Zhang, *Nanoscale*, 2016, **8**, 2510–2531.
7 G. Li and Z. Tang, *Nanoscale*, 2014, **6**, 3995–4011.
8 K. Mondal and A. Sharma, *RSC Adv.*, 2016, **6**, 83589–83612.
9 K. C. Ho and L. Y. Lin, *J. Mater. Chem. A*, 2019, **7**, 3516–3530.
10 M. Yusuf, S. Song, S. Park and K. H. Park, *Appl. Catal., A*, 2021, **613**, 118025.
11 A. Sivanantham, P. Ganesan, L. Estevez, B. P. McGrail, R. K. Motkuri and S. Shanmugam, *Adv. Energy Mater.*, 2018, **8**, 1702838.
12 R. G. Chaudhuri and S. Paria, *Chem. Rev.*, 2012, **112**, 2373–2433.
13 C. Wang, N. M. Markovic and V. R. Stamenkovic, *ACS Catal.*, 2012, **2**, 891–898.
14 N. V. Long, M. Ohtaki, T. D. Hien, J. Randy and M. Nogami, *Electrochim. Acta*, 2011, **56**, 9133–9143.
15 M. Sun, H. Liu, J. Qu and J. Li, *Adv. Energy Mater.*, 2016, **6**, 1600087.
16 Y. Shabangoli, M. S. Rahmanifar, M. F. El-Kady, A. Noori, M. F. Mousavi and R. B. Kaner, *Energy Storage Mater.*, 2018, **11**, 282–293.
17 Q. Lu, J. Yu, X. Zou, K. Liao, P. Tan, W. Zhou, M. Ni and Z. Shao, *Adv. Funct. Mater.*, 2019, **29**, 1904481.
18 L. Wang, Y. Sun, S. Zhang, H. Di, Q. Liu, X. Du, Z. Li, K. Yang and S. Chen, *ChemElectroChem*, 2021, **8**, 4286–4295.
19 Z. Zhou, Y. Kong, H. Tan, Q. Huang, C. Wang, Z. Pei, H. Wang, Y. Liu, Y. Wang, S. Li, X. Liao, W. Yan and S. Zhao, *Adv. Mater.*, 2022, **34**, 2106541.
20 K. H. Wu, Y. Liu, X. Tan, Y. Liu, Y. Lin, X. Huang, Y. Ding, B. J. Su, B. Zhang, J. M. Chen, W. Yan, S. C. Smith, I. R. Gentle and S. Zhao, *Chem Catal.*, 2022, **2**, 372–385.
21 Z. Jian, P. Liu, F. Li, P. He, X. Guo, M. Chen and H. Zhou, *Angew. Chem., Int. Ed.*, 2014, **53**, 442–446.

22 Y. Zhou, Q. Huang, C. T. J. Low, R. I. Walton, T. McNally and C. Wan, *New J. Chem.*, 2019, **43**, 5632–5641.
23 X. Huang, X. Zou, Y. Meng, E. Mikmeková, H. Chen, D. Voiry, A. Goswami, M. Chhowalla and T. Asefa, *ACS Appl. Mater. Interfaces*, 2015, **7**, 1978–1986.
24 J.-C. Li, P.-X. Hou and C. Liu, *Small*, 2017, **13**, 1702002.
25 M. Li, J. Zhou, Y. G. Bi, S. Q. Zhou and C. H. Mo, *Chem. Eng. J.*, 2020, **383**, 123152.
26 Q. Abbas, R. Raza, I. Shabbir and A. G. Olabi, *J. Sci.: Adv. Mater. Devices*, 2019, **4**, 341–352.
27 Y. He, X. Han, Y. Du, B. Zhang and P. Xu, *Polymers*, 2016, **8**, 366.
28 X. Wang, G. Sun, P. Routh, D. H. Kim, W. Huang and P. Chen, *Chem. Soc. Rev.*, 2014, **43**, 7067–7098.
29 G. L. Chai, K. Qiu, M. Qiao, M. M. Titirici, C. Shang and Z. Guo, *Energy Environ. Sci.*, 2017, **10**, 1186–1195.
30 A. Sarapuu, E. Kibena-Põldsepp, M. Borghei and K. Tammeveski, *J. Mater. Chem. A*, 2018, **6**, 776–804.
31 H. Cui, Z. Zhou and D. Jia, *Mater. Horiz.*, 2017, **4**, 7–19.
32 N. Mansor, T. S. Miller, I. Dedigama, A. B. Jorge, J. Jia, V. Brázdová, C. Mattevi, C. Gibbs, D. Hodgson, P. R. Shearing, C. A. Howard, F. Corà, M. Shaffer, D. J. L. Brett and P. F. McMillan, *Electrochim. Acta*, 2016, **222**, 44–57.
33 Z. Song, N. Cheng, A. Lushington and X. Sun, *Catalysts*, 2016, **6**, 116.
34 Z. Cui, G. Fu, Y. Li and J. B. Goodenough, *Angew. Chem., Int. Ed.*, 2017, **56**, 9901–9905.
35 H. P. Feng, L. Tang, G. M. Zeng, Y. Zhou, Y. C. Deng, X. Ren, B. Song, C. Liang, M. Y. Wei and J. F. Yu, *Adv. Colloid Interface Sci.*, 2019, **267**, 26–46.
36 D. T. Tran, T. Kshetri, D. C. Nguyen, J. Gautam, V. H. Hoa, H. T. Le, N. H. Kim and J. H. Lee, *Nano Today*, 2018, **22**, 100–131.
37 X. Bai, D. Cao and H. Zhang, *Inorg. Chem. Front.*, 2020, **7**, 411–420.
38 Y. Zhao, Q. Lai, J. Zhu, J. Zhong, Z. Tang, Y. Luo and Y. Liang, *Small*, 2018, **14**, 1704207.
39 J. Zhang, Z. Xia and L. Dai, *Sci. Adv.*, 2015, **1**, e1500564.
40 I. Staffell, D. Scamman, A. Velazquez Abad, P. Balcombe, P. E. Dodds, P. Ekins, N. Shah and K. R. Ward, *Energy Environ. Sci.*, 2019, **12**, 463–491.
41 L. Carrette, K. A. Friedrich and U. Stimming, *ChemPhysChem*, 2000, **1**, 162–193.
42 G. J. K. Acres, *J. Power Sources*, 2001, **100**, 60–66.
43 S. Guo and E. Wang, *Nano Today*, 2011, **6**, 240–264.
44 B. Cai, S. Henning, J. Herranz, T. J. Schmidt and A. Eychmüller, *Adv. Energy Mater.*, 2017, **7**, 1700548.
45 L. Shi, X. Lin, F. Liu, Y. Long, R. Cheng, C. Tan, L. Yang, C. Hu, S. Zhao and D. Liu, *ACS Catal.*, 2022, **12**, 5397–5406.
46 M. Yurukcu, E. O. Badradeen, S. Bilnoski, F. M. Yurtsever and M. Begum, *Mater. Sci. Eng. Int. J.*, 2018, **2**, 58–64.
47 K. Jiao and M. Ni, *Int. J. Energy Res.*, 2017, **41**, 1793–1797.
48 X. Wang, Z. Li, Y. Qu, T. Yuan, W. Wang, Y. Wu and Y. Li, *Chem*, 2019, **5**, 1486–1511.
49 X. Ren, Y. Wang, A. Liu, Z. Zhang, Q. Lv and B. Liu, *J. Mater. Chem. A*, 2020, **8**, 24284–24306.
50 M. S. Garapati and R. Sundara, *Int. J. Hydrogen Energy*, 2019, **44**, 10951–10963.
51 B. Fang, M.-S. Kim, J. H. Kim, M. Y. Song, Y.-J. Wang, H. Wang, D. P. Wilkinson and J.-S. Yu, *J. Mater. Chem.*, 2011, **21**, 8066–8073.
52 A. Kongkanand, N. P. Subramanian, Y. Yu, Z. Liu, H. Igarashi and D. A. Muller, *ACS Catal.*, 2016, **6**, 1578–1583.
53 K. Jiao, J. Xuan, Q. Du, Z. Bao, B. Xie, B. Wang, Y. Zhao, L. Fan, H. Wang, Z. Hou, S. Huo, N. P. Brandon, Y. Yin and M. D. Guiver, *Nature*, 2021, **595**, 361–369.
54 R. Jiang, S. on Tung, Z. Tang, L. Li, L. Ding, X. Xi, Y. Liu, L. Zhang and J. Zhang, *Energy Storage Mater.*, 2018, **12**, 260–276.
55 R. Lin, C. Cao, T. Zhao, Z. Huang, B. Li, A. Wieckowski and J. Ma, *J. Power Sources*, 2013, **223**, 190–198.
56 Y. J. Sa, C. Park, H. Y. Jeong, S. H. Park, Z. Lee, K. T. Kim, G. G. Park and S. H. Joo, *Angew. Chem., Int. Ed.*, 2014, **126**, 4186–4190.
57 J. S. Walker, N. V. Rees and P. M. Mendes, *J. Exp. Nanosci.*, 2018, **13**, 258–271.
58 S. J. Hwang, S. J. Yoo, J. Shin, Y. H. Cho, J. H. Jang, E. Cho, Y. E. Sung, S. W. Nam, T. H. Lim, S. C. Lee and S. K. Kim, *Sci. Rep.*, 2013, **3**, 1309.
59 M. Karuppannan, Y. Kim, S. Gok, E. Lee, J. Y. Hwang, J.-H. Jang, Y.-H. Cho, T. Lim, Y.-E. Sung and O. J. Kwon, *Energy Environ. Sci.*, 2019, **12**, 2820–2829.
60 H. Wu, D. Wexler, G. Wang and H. Liu, *J. Solid State Electrochem.*, 2012, **16**, 1105–1110.
61 C. Y. Ahn, J. Y. Cheon, S. H. Joo and J. Kim, *J. Power Sources*, 2013, **222**, 477–482.
62 K. Mohanraju, G. Kousik and L. Cindrella, *New J. Chem.*, 2016, **40**, 8681–8695.
63 D. J. You, D. H. Kim, J. R. De Lile, C. Li, S. G. Lee, J. M. Kim and C. Pak, *Appl. Catal., A*, 2018, **562**, 250–257.
64 G. Samjeské, S. Nagamatsu, S. Takao, K. Nagasawa, Y. Imaizumi, O. Sekizawa, T. Yamamoto, Y. Uemura, T. Uruga and Y. Iwasawa, *Phys. Chem. Chem. Phys.*, 2013, **15**, 17208–17218.
65 W.-Y. Huang, M.-Y. Chang, Y.-Z. Wang, Y.-C. Huang, K.-S. Ho, T.-H. Hsieh and Y.-C. Kuo, *Polymers*, 2020, **12**, 617.
66 M. Luo, L. Wei, F. Wang, K. Han and H. Zhu, *J. Power Sources*, 2014, **270**, 34–41.
67 Y. Xue, H. Li, X. Ye, S. Yang, Z. Zheng, X. Han, X. Zhang, L. Chen, Z. Xie, Q. Kuang and L. Zheng, *Nano Res.*, 2019, **12**, 2490–2497.
68 J. C. Douglin, J. R. Varcoe and D. R. Dekel, *J. Power Sources Adv.*, 2020, **5**, 100023.
69 S. Gottesfeld, D. R. Dekel, M. Page, C. Bae, Y. Yan, P. Zelenay and Y. S. Kim, *J. Power Sources*, 2018, **375**, 170–184.
70 W. E. Mustain, M. Chatenet, M. Page and Y. S. Kim, *Energy Environ. Sci.*, 2020, **13**, 2805–2838.
71 D. Henkensmeier, M. Najibah, C. Harms, J. Žitka, J. Hnát and K. Bouzek, *J. Electrochem. Energy Convers. Storage*, 2021, **18**, 024001.
72 H. S. Dang, E. A. Weiber and P. Jannasch, *J. Mater. Chem. A*, 2015, **3**, 5280–5284.

73 J. Ponce-González, D. K. Whelligan, L. Wang, R. Bance-Soualhi, Y. Wang, Y. Peng, H. Peng, D. C. Apperley, H. N. Sarode, T. P. Pandey, A. G. Divekar, S. Seifert, A. M. Herring, L. Zhuang and J. R. Varcoe, *Energy Environ. Sci.*, 2016, **9**, 3724–3735.
74 Y. J. Sa, C. Park, H. Y. Jeong, S. H. Park, Z. Lee, K. T. Kim, G. G. Park and S. H. Joo, *Angew. Chem., Int. Ed.*, 2014, **53**, 4102–4106.
75 D. W. Lee, J. H. Jang, I. Jang, Y. S. Kang, S. Jang, K. Y. Lee, J. H. Jang, H. J. Kim and S. J. Yoo, *Small*, 2019, **15**, 1902090.
76 J. Woo, S. Y. Yang, Y. J. Sa, W. Y. Choi, M. H. Lee, H. W. Lee, T. J. Shin, T. Y. Kim and S. H. Joo, *Chem. Mater.*, 2018, **30**, 6684–6701.
77 D. S. Baek, K. A. Lee, J. Park, J. H. Kim, J. Lee, J. S. Lim, S. Y. Lee, T. J. Shin, H. Y. Jeong, J. S. Son, S. J. Kang, J. Y. Kim and S. H. Joo, *Angew. Chem., Int. Ed.*, 2021, **60**, 1441–1449.
78 V. Vijayakumar and S. Y. Nam, *J. Ind. Eng. Chem.*, 2019, **70**, 70–86.
79 N. Ramaswamy and S. Mukerjee, *Chem. Rev.*, 2019, **119**, 11945–11979.
80 F. Xu, Y. Su and B. Lin, *Front. Mater.*, 2020, 4.
81 S. Ratso, I. Kruusenberg, M. Käärik, M. Kook, L. Puust, R. Saar, J. Leis and K. Tammeveski, *J. Power Sources*, 2018, **375**, 233–243.
82 D. R. Dekel, *J. Power Sources*, 2018, **375**, 158–169.
83 E. Negro, A. Bach Delpeuch, K. Vezzù, G. Nawn, F. Bertasi, A. Ansaldo, V. Pellegrini, B. Dembinska, S. Zoladek, K. Miecznikowski, I. A. Rutkowska, M. Skunik-Nuckowska, P. J. Kulesza, F. Bonaccorso and V. Di Noto, *Chem. Mater.*, 2018, **30**, 2651–2659.
84 Z. F. Pan, L. An, T. S. Zhao and Z. K. Tang, *Prog. Energy Combust. Sci.*, 2018, **66**, 141–175.
85 M. Hren, M. Božič, D. Fakin, K. S. Kleinschek and S. Gorgieva, *Sustainable Energy Fuels*, 2021, **5**, 604–637.
86 M. C. L. Santos, L. C. Nunes, L. M. G. Silva, A. S. Ramos, F. C. Fonseca, R. F. B. de Souza and A. O. Neto, *ChemistrySelect*, 2019, **4**, 11430–11434.
87 S. K. Singh, V. Kashyap, N. Manna, S. N. Bhange, R. Soni, R. Boukherroub, S. Szunerits and S. Kurungot, *ACS Catal.*, 2017, **7**, 6700–6710.
88 T. Palaniselvam, V. Kashyap, S. N. Bhange, J.-B. Baek and S. Kurungot, *Adv. Funct. Mater.*, 2016, **26**, 2150–2162.
89 S. Ratso, M. Käärik, M. Kook, P. Paiste, V. Kisand, S. Vlassov, J. Leis and K. Tammeveski, *ChemElectroChem*, 2018, **5**, 1827–1836.
90 H.-C. Huang, Y.-C. Lin, S.-T. Chang, C.-C. Liu, K.-C. Wang, H.-P. Jhong, J.-F. Lee and C.-H. Wang, *J. Mater. Chem. A*, 2017, **5**, 19790–19799.
91 M. M. Hossen, K. Artyushkova, P. Atanassov and A. Serov, *J. Power Sources*, 2018, **375**, 214–221.
92 H. Ren, Y. Wang, Y. Yang, X. Tang, Y. Peng, H. Peng, L. Xiao, J. Lu, H. D. Abruña and L. Zhuang, *ACS Catal.*, 2017, **7**, 6485–6492.
93 C. Chen, X.-D. Yang, Z.-Y. Zhou, Y.-J. Lai, M. Rauf, Y. Wang, J. Pan, L. Zhuang, Q. Wang, Y.-C. Wang, N. Tian, X.-S. Zhang and S.-G. Sun, *Chem. Commun.*, 2015, **51**, 17092–17095.
94 X. Li, B. N. Popov, T. Kawahara and H. Yanagi, *J. Power Sources*, 2011, **196**, 1717–1722.
95 C. V. Rao and Y. Ishikawa, *J. Phys. Chem. C*, 2012, **116**, 4340–4346.
96 S. M. Unni, S. N. Bhange, R. Illathvalappil, N. Mutneja, K. R. Patil and S. Kurungot, *Small*, 2015, **11**, 352–360.
97 S. M. Unni, S. Ramadas, R. Illathvalappil, S. N. Bhange and S. Kurungot, *J. Mater. Chem. A*, 2015, **3**, 4361–4367.
98 A. Yuda, A. Ashok and A. Kumar, *Catal. Rev.: Sci. Eng.*, 2020, **64**, 126–228.
99 A. Yuda and A. Kumar, *Int. J. Hydrogen Energy*, 2022, **47**, 3371–3395.
100 Y. Tong, X. Yan, J. Liang and S. X. Dou, *Small*, 2021, **17**, 1904126.
101 D. J. You, K. Kwon, S. H. Joo, J. H. Kim, J. M. Kim, C. Pak and H. Chang, *Int. J. Hydrogen Energy*, 2012, **37**, 6880–6885.
102 A. Glüsen, F. Dionigi, P. Paciok, M. Heggen, M. Müller, L. Gan, P. Strasser, R. E. Dunin-Borkowski and D. Stolten, *ACS Catal.*, 2019, **9**, 3764–3772.
103 Z. Wen, J. Liu and J. Li, *Adv. Mater.*, 2008, **20**, 743–747.
104 S. H. Joo, K. Kwon, D. J. You, C. Pak, H. Chang and J. M. Kim, *Electrochim. Acta*, 2009, **54**, 5746–5753.
105 N. Jha, A. Leela Mohana Reddy, M. M. Shaijumon, N. Rajalakshmi and S. Ramaprabhu, *Int. J. Hydrogen Energy*, 2008, **33**, 427–433.
106 Y. Zhang, X. Zhang, X. Ma, W. Guo, C. Wang, T. Asefa and X. He, *Sci. Rep.*, 2017, **7**, 43366.
107 N. Bhandary, P. P. Ingole and S. Basu, *ChemistrySelect*, 2017, **2**, 8151–8157.
108 Q. Liu and J. Zhang, *Langmuir*, 2013, **29**, 3821–3828.
109 M. G. Hosseini, R. Mahmoodi and V. Daneshvari-Esfahlan, *Energy*, 2018, **161**, 1074–1084.
110 N. Muthuswamy, J. L. G. De La Fuente, D. T. Tran, J. Walmsley, M. Tsypkin, S. Raaen, S. Sunde, M. Rønning and D. Chen, *Int. J. Hydrogen Energy*, 2013, **38**, 16631–16641.
111 Z. Y. Shih, Z. Yang, Z. H. Lin and H. T. Chang, *Int. J. Hydrogen Energy*, 2011, **36**, 7303–7309.
112 Q. Tan, C. Du, G. Yin, P. Zuo, X. Cheng and M. Chen, *J. Catal.*, 2012, **295**, 217–222.
113 W. Yang, Q. Zhang, C. Peng, E. Wu, S. Chen, Y. Ma, J. Hou, Y. He, B. Zhang and L. Deng, *RSC Adv.*, 2019, **9**, 931–939.
114 Z. L. Zhao, L. Y. Zhang, S. J. Bao and C. M. Li, *Appl. Catal., B*, 2015, **174–175**, 361–366.
115 L. Jin, H. Xu, C. Chen, H. Shang, Y. Wang, C. Wang and Y. Du, *ACS Appl. Mater. Interfaces*, 2019, **11**, 42123–42130.
116 H. Wang, R. Wang, H. Li, Q. Wang, J. Kang and Z. Lei, *Int. J. Hydrogen Energy*, 2011, **36**, 839–848.
117 Y. Yang, C. Tan, Y. Yang, L. Zhang, B. Zhang, K. Wu and S. Zhao, *ChemCatChem*, 2021, **13**, 1587–1594.
118 T. Kwon, M. Jun, H. Y. Kim, A. Oh, J. Park, H. Baik, S. H. Joo and K. Lee, *Adv. Funct. Mater.*, 2018, **28**, 1706440.
119 T. H. Ko, K. Devarayan, M. K. Seo, H. Y. Kim and B. S. Kim, *Sci. Rep.*, 2016, **6**, 20313.

120 X. Yu, L. Kuai and B. Geng, *Nanoscale*, 2012, **4**, 5738–5743.
121 V. Parthiban, S. Akula, S. G. Peera, N. Islam and A. K. Sahu, *Energy Fuels*, 2015, **30**, 725–734.
122 V. Parthiban, S. Akula and A. K. Sahu, *J. Membr. Sci.*, 2017, **541**, 127–136.
123 M. S. Çögenli and A. Bayrakçeken Yurtcan, *Int. J. Hydrogen Energy*, 2020, **45**, 650–666.
124 D. Lee, S. Gok, Y. Kim, Y. E. Sung, E. Lee, J. H. Jang, J. Y. Hwang, O. J. Kwon and T. Lim, *ACS Appl. Mater. Interfaces*, 2020, **12**, 44588–44596.
125 Y. Feng, H. Liu and J. Yang, *Sci. Adv.*, 2017, **3**, e170058.
126 K. Kang, G. Lee, G. Gwak, Y. Choi and H. Ju, *Int. J. Hydrogen Energy*, 2012, **37**, 6285–6291.
127 Y. S. Kim, D. H. Peck, S. K. Kim, D. H. Jung, S. Lim and S. H. Kim, *Int. J. Hydrogen Energy*, 2013, **38**, 7159–7168.
128 B. Yao, X. Yan, Y. Ding, Z. Lu, D. Dong, H. Ishida, M. Litt and L. Zhu, *Macromolecules*, 2014, **47**, 1039–1045.
129 A. Paneri, Y. Heo, G. Ehlert, A. Cottrill, H. Sodano, P. Pintauro and S. Moghaddam, *J. Membr. Sci.*, 2014, **467**, 217–225.
130 W. Yuan, J. Deng, Z. Zhang, X. Yang and Y. Tang, *Renewable Energy*, 2014, **62**, 640–648.
131 J. Liu, Y. Zheng, Z. Hong, K. Cai, F. Zhao and H. Han, *Sci. Adv.*, 2016, **2**, e1600858.
132 N. Tian, Z. Y. Zhou, S. G. Sun, Y. Ding and L. W. Zhong, *Science*, 2007, **316**, 732–735.
133 G. Yang, Z. Zhang, X. Kang, L. Li, Y. Li and Y. Sun, *ACS Appl. Energy Mater.*, 2020, **3**, 11929–11938.
134 X. Luo, W. Han, W. Du, Z. Huang, Y. Jiang and Y. Zhang, *J. Power Sources*, 2020, **469**, 228184.
135 J. Liu, L. Wei, C. Cao, F. Zhang, F. Lang, H. Wang, H. Yang and J. Shen, *Nanoscale*, 2019, **11**, 13431–13439.
136 M. Zhang, Z. Ma and H. Song, *Nanomaterials*, 2021, **11**, 377.
137 D. Wang, J. Hu, J. Yang, K. Xiao, S. Liang, J. Xu, B. Liu and H. Hou, *Int. J. Hydrogen Energy*, 2020, **45**, 3163–3175.
138 W. Han, C. Li, Y. Jiang, Z. Ma, Y. Zhang, X. Yan and X. Zheng, *J. Alloys Compd.*, 2021, **852**, 156994.
139 J. Ji, J. Woo, Y. Chung, S. H. Joo and Y. Kwon, *Chem. Eng. J.*, 2020, **381**, 122679.
140 G. Yang, D. Chen, P. Lv, X. Kong, Y. Sun, Z. Wang, Z. Yuan, H. Liu and J. Yang, *Sci. Rep.*, 2016, **6**, 35252.
141 S. Zhong, L. Zhou, L. Wu, L. Tang, Q. He and J. Ahmed, *J. Power Sources*, 2014, **272**, 344–350.
142 W. Yang, Y. Dong, J. Li, Q. Fu and L. Zhang, *Int. J. Hydrogen Energy*, 2021, **46**, 2530–2542.
143 L. Jiang, J. Chen, D. Han, S. Chang, R. Yang, Y. An, Y. Liu and F. Chen, *J. Power Sources*, 2020, **453**, 227877.
144 Y. Xu, S. Zhou and M. Li, *Int. J. Hydrogen Energy*, 2019, **44**, 13875–13884.
145 Q. Liu, Y. Zhou, S. Chen, Z. Wang, H. Hou and F. Zhao, *J. Power Sources*, 2015, **273**, 1189–1193.
146 Y. Zou, J. Li, Q. Fu, L. Zhang, Q. Liao and X. Zhu, *Electrochim. Acta*, 2019, **320**, 134590.
147 C. Cao, L. Wei, G. Wang, J. Liu, Q. Zhai and J. Shen, *Inorg. Chem. Front.*, 2017, **4**, 1930–1938.
148 B. Mecheri, R. Gokhale, C. Santoro, M. A. C. de Oliveira, A. D'Epifanio, S. Licoccia, A. Serov, K. Artyushkova and P. Atanassov, *ACS Appl. Energy Mater.*, 2018, **1**, 5755–5765.
149 L. Zhou, C. Yang, J. Wen, P. Fu, Y. Zhang, J. Sun, H. Wang and Y. Yuan, *J. Mater. Chem. A*, 2017, **5**, 19343–19350.
150 R. Li, Y. Dai, B. Chen, J. Zou, B. J. Jiang and H. Fu, *J. Power Sources*, 2016, **307**, 1–10.
151 Y. Liu, Y. S. Fan and Z. M. Liu, *Chem. Eng. J.*, 2019, **361**, 416–427.
152 X. Tian, M. Zhou, C. Tan, M. Li, L. Liang, K. Li and P. Su, *Chem. Eng. J.*, 2018, **348**, 775–785.
153 P. Ren, S. Ci, Y. Ding and Z. Wen, *Appl. Surf. Sci.*, 2019, **481**, 1206–1212.
154 X. Shi, J. Zhang and T. Huang, *Energy Technol.*, 2017, **5**, 1712–1719.
155 M. T. Nguyen, B. Mecheri, A. Iannaci, A. D'Epifanio and S. Licoccia, *Electrochim. Acta*, 2016, **190**, 388–395.
156 Y. E. Song, S. Lee, M. Kim, J. G. Na, J. Lee, J. Lee and J. R. Kim, *J. Power Sources*, 2020, **451**, 227816.
157 N. T. Q. Tran, H. S. Gil, G. Das, B. H. Kim and H. H. Yoon, *Korean Chem. Eng. Res.*, 2019, **57**, 387–391.
158 N. Senthilkumar, G. G. Kumar and A. Manthiram, *Adv. Energy Mater.*, 2018, **8**, 1702207.
159 J. Cao, Z. Zhu, W. Zhao, J. Xu and Z. Chen, *Chin. J. Chem.*, 2016, **34**, 1086–1092.
160 X. J. Zhang, J. M. Zhang, P. Y. Zhang, Y. Li, S. Xiang, H. G. Tang and Y. J. Fan, *Mol. Catal.*, 2017, **436**, 138–144.
161 Y. Kang, L. Qi, M. Li, R. E. Diaz, D. Su, R. R. Adzic, E. Stach, J. Li and C. B. Murray, *ACS Nano*, 2012, **6**, 2818–2825.
162 S. S. Hossain, *Int. J. Electrochem. Sci.*, 2021, **16**, 150926.
163 R. R. Kapaev, F. A. Obrezkov, K. J. Stevenson and P. A. Troshin, *Chem. Commun.*, 2019, **55**, 11758–11761.
164 W. Zhang, M. Sun, J. Yin, E. Abou-Hamad, U. Schwingenschlögl, P. M. F. J. Costa and H. N. Alshareef, *Angew. Chem., Int. Ed.*, 2021, **60**, 1355–1363.
165 J. J. Shea and C. Luo, *ACS Appl. Mater. Interfaces*, 2020, **12**, 5361–5380.
166 W. Lu, X. Guo, Y. Luo, Q. Li, R. Zhu and H. Pang, *Chem. Eng. J.*, 2019, **355**, 208–237.
167 L. Trahey, F. R. Brushett, N. P. Balsara, G. Ceder, L. Cheng, Y. M. Chiang, N. T. Hahn, B. J. Ingram, S. D. Minteer, J. S. Moore, K. T. Mueller, L. F. Nazar, K. A. Persson, D. J. Siegel, K. Xu, K. R. Zavadil, V. Srinivasan and G. W. Crabtree, *Proc. Natl. Acad. Sci. U. S. A.*, 2020, **117**, 12550–12557.
168 D. Ganguly, A. P. Ajay, A. Ghosh and S. Ramaprabhu, *Sci. Rep.*, 2020, **10**, 9945.
169 L. Su, Y. Jing and Z. Zhou, *Nanoscale*, 2011, **3**, 3967–3983.
170 L. Shen, H. Li, E. Uchaker, X. Zhang and G. Cao, *Nano Lett.*, 2012, **12**, 5673–5678.
171 W. Zhou, J. Zhu, C. Cheng, J. Liu, H. Yang, C. Cong, C. Guan, X. Jia, H. J. Fan, Q. Yan, C. M. Li and T. Yu, *Energy Environ. Sci.*, 2011, **4**, 4954–4961.
172 G. Tan, F. Wu, Y. Yuan, R. Chen, T. Zhao, Y. Yao, J. Qian, J. Liu, Y. Ye, R. Shahbazian-Yassar, J. Lu and K. Amine, *Nat. Commun.*, 2016, **7**, 11774.

173 R. Rajagopal and K. S. Ryu, *J. Electroanal. Chem.*, 2020, **856**, 113669.
174 G. Jeong, J. G. Kim, M. S. Park, M. Seo, S. M. Hwang, Y. U. Kim, Y. J. Kim, J. H. Kim and S. X. Dou, *ACS Nano*, 2014, **8**, 2977–2985.
175 L. Gao, F. Qu and X. Wu, *J. Mater. Chem. A*, 2014, **2**, 7367–7372.
176 S. Lee, J. Ha, H. Cheng, J. W. Lee, T. S. Jang, Y. G. Jung, Y. Huang, J. A. Rogers and U. Paik, *Adv. Energy Mater.*, 2014, **4**, 1300472.
177 H. Liu, Z. Li, Y. Liang, R. Fu and D. Wu, *Carbon*, 2015, **84**, 419–425.
178 L. Thirugnanam, M. Palanisamy, S. Kaveri, S. Ramaprabhu, V. G. Pol and M. Dutta, *Int. J. Hydrogen Energy*, 2021, **46**, 2464–2478.
179 W. Hua, B. Schwarz, R. Azmi, M. Müller, M. S. Dewi Darma, M. Knapp, A. Senyshyn, M. Heere, A. Missyul, L. Simonelli, J. R. Binder, S. Indris and H. Ehrenberg, *Nano Energy*, 2020, **78**, 105231.
180 L. Liang, Y. Xu, L. Wen, Y. Li, M. Zhou, C. Wang, H. Zhao, U. Kaiser and Y. Lei, *Nano Res.*, 2017, **10**, 3189–3201.
181 C. Wu, X. Tong, Y. Ai, D. S. Liu, P. Yu, J. Wu and Z. M. Wang, *Nano-Micro Lett.*, 2018, **10**, 40.
182 R. Chandrabhan Shende, P. Chandran and S. Ramaprabhu, *Nanotechnology*, 2020, **31**, 235403.
183 Z. Xiong, D. Sun, X. Jia and J. Zhou, *Carbon*, 2020, **166**, 339–349.
184 S.-Y. Duan, J.-Y. Piao, T.-Q. Zhang, Y.-G. Sun, X.-C. Liu, A.-M. Cao and L.-J. Wan, *NPG Asia Mater.*, 2017, **9**, e414.
185 A. P. Vijaya Kumar Saroja, M. S. Garapati, R. ShyiamalaDevi, M. Kamaraj and S. Ramaprabhu, *Appl. Surf. Sci.*, 2020, **504**, 144430.
186 F. Kong, Z. Han, S. Tao and B. Qian, *J. Energy Chem.*, 2021, **55**, 256–264.
187 C. Chen, Z. Han, S. Chen, S. Qi, X. Lan, C. Zhang, L. Chen, P. Wang and W. Wei, *ACS Appl. Mater. Interfaces*, 2020, **12**, 7144–7152.
188 J. Yin, Y. Shen, C. Li, C. Fan, S. Sun, Y. Liu, J. Peng, L. Qing and J. Han, *ChemSusChem*, 2019, **12**, 4786–4790.
189 W. Zhao, C. Guo and C. M. Li, *J. Mater. Chem. A*, 2017, **5**, 19195–19202.
190 Y. Mei, Y. Huang and X. Hu, *J. Mater. Chem. A*, 2016, **4**, 12001–12013.
191 Y. L. Bai, R. Xarapatgvl, X. Y. Wu, X. Liu, Y. S. Liu, K. X. Wang and J. S. Chen, *Nanoscale*, 2019, **11**, 17860–17868.
192 B. Ji, W. Yao, Y. Zheng, P. Kidkhunthod, X. Zhou, S. Tunmee, S. Sattayaporn, H.-M. Cheng, H. He and Y. Tang, *Nat. Commun.*, 2020, **11**, 1225.
193 Y. He, Y. Xu, J. Li, Z. Xu, Z. Zhang, J. Sun, M. Zhang, X. Zhu and X. Zhou, *Energy Fuels*, 2021, **35**, 3490–3496.
194 J. Bao, W. Deng, J. Liu and C.-F. Sun, *Energy Storage Mater.*, 2021, **42**, 806–814.
195 H. Sun, P. Liang, G. Zhu, W. H. Hung, Y.-Y. Li, H.-C. Tai, C.-L. Huang, J. Li, Y. Meng, M. Angell, C.-A. Wang and H. Dai, *Proc. Natl. Acad. Sci. U. S. A.*, 2020, **117**, 27847–27853.
196 C. Zhang, Y. Xu, M. Zhou, L. Liang, H. Dong, M. Wu, Y. Yang and Y. Lei, *Adv. Funct. Mater.*, 2017, **27**, 1604307.
197 Y. Zhu, Y. Yin, X. Yang, T. Sun, S. Wang, Y. Jiang, J. Yan and X. Zhang, *Angew. Chem., Int. Ed.*, 2017, **56**, 7881–7885.
198 Y. Xu, F. Bahmani, M. Zhou, Y. Li, C. Zhang, F. Liang, S. H. Kazemi, U. Kaiser, G. Meng and Y. Lei, *Nanoscale Horiz.*, 2018, **4**, 202–207.
199 L. Deng, T. Wang, Y. Hong, M. Feng, R. Wang, J. Zhang, Q. Zhang, J. Wang, L. Zeng, Y. Zhu and L. Guo, *ACS Energy Lett.*, 2020, **5**, 1916–1922.
200 W. Wang, B. Jiang, C. Qian, F. Lv, J. Feng, J. Zhou, K. Wang, C. Yang, Y. Yang and S. Guo, *Adv. Mater.*, 2018, **30**, 1801812.
201 S. H. Yang, S.-K. Park and Y. C. Kang, *Nano-Micro Lett.*, 2021, **13**, 9.
202 J. Chu, Q. Yu, D. Yang, L. Xing, C. Y. Lao, M. Wang, K. Han, Z. Liu, L. Zhang, W. Du, K. Xi, Y. Bao and W. (Alex) Wang, *Appl. Mater. Today*, 2018, **13**, 344–351.
203 Y. Luo, M. Tao, J. Deng, R. Zhan, B. Guo, Q. Ma, M. K. Aslam, Y. Qi and M. Xu, *Inorg. Chem. Front.*, 2020, **7**, 394–401.
204 H. Ren, C. Gu, J. Zhao, S. W. Joo and J. Huang, *Appl. Surf. Sci.*, 2019, **473**, 918–927.
205 R. Mo, D. Rooney, K. Sun and H. Y. Yang, *Nat. Commun.*, 2017, **8**, 13949.
206 J. H. Kim and Y. C. Kang, *Small*, 2017, **13**, 1701585.
207 J. Guo, H. Zhu, Y. Sun, L. Tang and X. Zhang, *J. Mater. Chem. A*, 2016, **4**, 4783–4789.
208 J. Ma, H. Zhang, Y. Xin, S. Liu, Y. Li, L. Yang, G. Xu, T. Lou, H. Niu and S. Yang, *Dalton Trans.*, 2021, **50**, 1703–1711.
209 S. Liu, J. Wang, J. Wang, F. Zhang and L. Wang, *Appl. Surf. Sci.*, 2016, **390**, 86–91.
210 Y. Ding, Z.-F. Li, E. V. Timofeeva and C. U. Segre, *Adv. Energy Mater.*, 2018, **8**, 1702134.
211 K.-H. Kim, W.-S. Kim and S.-H. Hong, *Nanoscale*, 2019, **11**, 13494–13501.
212 J. Yang, Y. Ouyang, H. Zhang, H. Xu, Y. Zhang and Y. Wang, *J. Mater. Chem. A*, 2016, **4**, 9923–9930.
213 C. Wu, P. Kopold, P. A. van Aken, J. Maier and Y. Yu, *Adv. Mater.*, 2017, **29**, 1604015.
214 J. Fullenwarth, A. Darwiche, A. Soares, B. Donnadieu and L. Monconduit, *J. Mater. Chem. A*, 2014, **2**, 2050–2059.
215 R. Zhang, V. Raveendran, Y. He, A. Yau, A. Chang, C. Chi, S. Bong, F. Cheng, W. Ma and J. Chen, *Energy Mater. Adv.*, 2021, **2021**, 2124862.
216 Y. Kim, Y. Kim, A. Choi, S. Woo, D. Mok, N.-S. Choi, Y. S. Jung, J. H. Ryu, S. M. Oh and K. T. Lee, *Adv. Mater.*, 2014, **26**, 4139–4144.
217 L. Ma, P. Yan, S. Wu, G. Zhu and Y. Shen, *J. Mater. Chem. A*, 2017, **5**, 16994–17000.
218 X. Ge, Z. Li and L. Yin, *Nano Energy*, 2017, **32**, 117–124.
219 J. Wang, B. Wang, X. Liu, G. Wang, H. Wang and J. Bai, *J. Colloid Interface Sci.*, 2019, **538**, 187–198.
220 Z. Liu, T. Lu, T. Song, X.-Y. Yu, X. W. (David) Lou and U. Paik, *Energy Environ. Sci.*, 2017, **10**, 1576–1580.
221 Y. Jiang, Y. Feng, B. Xi, S. Kai, K. Mi, J. Feng, J. Zhang and S. Xiong, *J. Mater. Chem. A*, 2016, **4**, 10719–10726.

222 Q. Zhou, L. Liu, Z. Huang, L. Yi, X. Wang and G. Cao, *J. Mater. Chem. A*, 2016, **4**, 5505–5516.
223 S. Y. Lee and Y. C. Kang, *Chem. – Eur. J.*, 2016, **22**, 2769–2774.
224 A. Mahmood, S. Li, Z. Ali, H. Tabassum, B. Zhu, Z. Liang, W. Meng, W. Aftab, W. Guo, H. Zhang, M. Yousaf, S. Gao, R. Zou and Y. Zhao, *Adv. Mater.*, 2019, **31**, 1805430.
225 Q. Tan, P. Li, K. Han, Z. Liu, Y. Li, W. Zhao, D. He, F. An, M. Qin and X. Qu, *J. Mater. Chem. A*, 2019, **7**, 744–754.
226 W. Zhang, W. Miao, X. Liu, L. Li, Z. Yu and Q. Zhang, *J. Alloys Compd.*, 2018, **769**, 141–148.
227 Y. Han, W. Li, K. Zhou, X. Wu, H. Wu, X. Wu, Q. Shi, G. Diao and M. Chen, *ChemNanoMat*, 2020, **6**, 132–138.
228 D. Li, X. Ren, Q. Ai, Q. Sun, L. Zhu, Y. Liu, Z. Liang, R. Peng, P. Si, J. Lou, J. Feng and L. Ci, *Adv. Energy Mater.*, 2018, **8**, 1802386.
229 F. Cheng and J. Chen, *Chem. Soc. Rev.*, 2012, **41**, 2172–2192.
230 C. Wang, Y. Yu, J. Niu, Y. Liu, D. Bridges, X. Liu, J. Pooran, Y. Zhang and A. Hu, *Appl. Sci.*, 2019, **9**, 2787.
231 Y. Li and J. Lu, *ACS Energy Lett.*, 2017, **2**, 1370–1377.
232 A. Kraytsberg and Y. Ein-Eli, *Nano Energy*, 2013, **2**, 468–480.
233 K. Song, J. Jung, M. Park, H. Park, H. J. Kim, S. Il Choi, J. Yang, K. Kang, Y. K. Han and Y. M. Kang, *ACS Catal.*, 2018, **10**, 9006–9015.
234 Z. Ma, X. Yuan, L. Li, Z. F. Ma, D. P. Wilkinson, L. Zhang and J. Zhang, *Energy Environ. Sci.*, 2015, **8**, 2144–2198.
235 S. Y. Kim, H. T. Lee and K. B. Kim, *Phys. Chem. Chem. Phys.*, 2013, **15**, 20262–20271.
236 D. U. Lee, M. G. Park, Z. P. Cano, W. Ahn and Z. Chen, *ChemSusChem*, 2018, **11**, 406–414.
237 M. J. Song and M. W. Shin, *Appl. Surf. Sci.*, 2014, **320**, 435–440.
238 C. Tang, Y. Mao, J. Xie, Z. Chen, J. Tu, G. Cao and X. Zhao, *Inorg. Chem. Front.*, 2018, **5**, 1707–1713.
239 S. Peng, Y. Hu, L. Li, X. Han, F. Cheng, M. Srinivasan, Q. Yan, S. Ramakrishna and J. Chen, *Nano Energy*, 2015, **13**, 718–726.
240 A. Kondori, Z. Jiang, M. Esmaeilirad, M. Tamadoni Saray, A. Kakekhani, K. Kucuk, P. Navarro Munoz Delgado, S. Maghsoudipour, J. Hayes, C. S. Johnson, C. U. Segre, R. Shahbazian-Yassar, A. M. Rappe and M. Asadi, *Adv. Mater.*, 2020, **32**, 2004028.
241 H. Wang, F. Yin, P. Lv, T. Fan, X. He and B. Chen, *Int. J. Hydrogen Energy*, 2017, **42**, 2127–2133.
242 P. Gu, M. Zheng, Q. Zhao, X. Xiao, H. Xue and H. Pang, *J. Mater. Chem. A*, 2017, **5**, 7651–7666.
243 W. Sun, F. Wang, B. Zhang, M. Zhang, V. Küpers, X. Ji, C. Theile, P. Bieker, K. Xu, C. Wang and M. Winter, *Science*, 2021, **371**, 46–51.
244 J. S. Lee, S. T. Kim, R. Cao, N. S. Choi, M. Liu, K. T. Lee and J. Cho, *Adv. Energy Mater.*, 2011, **1**, 34–50.
245 Z. Wang, J. Huang, L. Wang, Y. Liu, W. Liu, S. Zhao and Z. Q. Liu, *Angew. Chem., Int. Ed.*, 2022, **61**, e202114696.
246 X. Lu, H. M. Chan, C. L. Sun, C. M. Tseng and C. Zhao, *J. Mater. Chem. A*, 2015, **3**, 13371–13376.
247 Z. Wang, Y. Lu, Y. Yan, T. Y. P. Larissa, X. Zhang, D. Wuu, H. Zhang, Y. Yang and X. Wang, *Nano Energy*, 2016, **30**, 368–378.
248 M. Wang, Y. Liu, K. Zhang, F. Yu, F. Qin, J. Fang, Y. Lai and J. Li, *RSC Adv.*, 2016, **6**, 83386–83392.
249 Y. Cheng, S. Dou, J. P. Veder, S. Wang, M. Saunders and S. P. Jiang, *ACS Appl. Mater. Interfaces*, 2017, **9**, 8121–8133.
250 Z. Guo, F. Wang, Y. Xia, J. Li, A. G. Tamirat, Y. Liu, L. Wang, Y. Wang and Y. Xia, *J. Mater. Chem. A*, 2018, **6**, 1443–1453.
251 X. Liu, L. Wang, P. Yu, C. Tian, F. Sun, J. Ma, W. Li and H. Fu, *Angew. Chem., Int. Ed.*, 2018, **57**, 16166–16170.
252 W. Fang, H. Hu, T. Jiang, G. Li and M. Wu, *Carbon*, 2019, **146**, 476–485.
253 S. Ibraheem, S. Chen, J. Li, Q. Wang and Z. Wei, *J. Mater. Chem. A*, 2019, **7**, 9497–9502.
254 J. Zhang, M. Zhang, L. Qiu, Y. Zeng, J. Chen, C. Zhu, Y. Yu and Z. Zhu, *J. Mater. Chem. A*, 2019, **7**, 19045–19059.
255 W. Xie, J. Li, Y. Song, S. Li, J. Li and M. Shao, *Nano-Micro Lett.*, 2020, **12**, 97.
256 F. Wang, H. Zhao, Y. Ma, Y. Yang, B. Li, Y. Cui, Z. Guo and L. Wang, *J. Energy Chem.*, 2020, **50**, 52–62.
257 J. Jiao, Y. Pan, B. Wang, W. Yang, S. Liu and C. Zhang, *J. Energy Chem.*, 2020, **53**, 364–371.
258 Q. Zhou, Z. Zhang, J. Cai, B. Liu, Y. Zhang, X. Gong, X. Sui, A. Yu, L. Zhao, Z. Wang and Z. Chen, *Nano Energy*, 2020, **71**, 104592.
259 T. T. Gebremariam, F. Chen, Q. Wang, J. Wang, Y. Liu, X. Wang and A. Qaseem, *ACS Appl. Energy Mater.*, 2018, **1**, 1612–1625.
260 K. Chen, S. Kim, R. Rajendiran, K. Prabakar, G. Li, Z. Shi, C. Jeong, J. Kang and O. L. Li, *J. Colloid Interface Sci.*, 2021, **582**, 977–990.
261 R. Zhao, Q. Li, Z. Chen, V. Jose, X. Jiang, G. Fu, J.-M. Lee and S. Huang, *Carbon*, 2020, **164**, 398–406.
262 R. Zhao, J. Chen, Z. Chen, X. Jiang, G. Fu, Y. Tang, W. Jin, J.-M. Lee and S. Huang, *ACS Appl. Energy Mater.*, 2020, **3**, 4539–4548.
263 F. Meng, H. Zhong, D. Bao, J. Yan and X. Zhang, *J. Am. Chem. Soc.*, 2016, **138**, 10226–10231.
264 X. Han, X. Ling, Y. Wang, T. Ma, C. Zhong, W. Hu and Y. Deng, *Angew. Chem., Int. Ed.*, 2019, **58**, 5359–5364.
265 C.-Y. Su, H. Cheng, W. Li, Z.-Q. Liu, N. Li, Z. Hou, F.-Q. Bai, H.-X. Zhang and T.-Y. Ma, *Adv. Energy Mater.*, 2017, **7**, 1602420.
266 K. Sheng, Q. Yi, A.-L. Chen, Y. Wang, Y. Yan, H. Nie and X. Zhou, *ACS Appl. Mater. Interfaces*, 2021, **13**, 45394–45405.
267 Y. Xu, P. Deng, G. Chen, J. Chen, Y. Yan, K. Qi, H. Liu and B. Y. Xia, *Adv. Funct. Mater.*, 2020, **30**, 1906081.
268 A. I. Douka, Y. Xu, H. Yang, S. Zaman, Y. Yan, H. Liu, M. A. Salam and B. Y. Xia, *Adv. Mater.*, 2020, **32**, 2002170.
269 W. Wan, X. Liu, H. Li, X. Peng, D. Xi and J. Luo, *Appl. Catal., B*, 2019, **240**, 193–200.
270 Q. Wang, Y. Ji, Y. Lei, Y. Wang, Y. Wang, Y. Li and S. Wang, *ACS Energy Lett.*, 2018, **3**, 1183–1191.
271 Y. Qiao, P. Yuan, Y. Hu, J. Zhang, S. Mu, J. Zhou, H. Li, H. Xia, J. He and Q. Xu, *Adv. Mater.*, 2018, **30**, 1804504.
272 Y.-W. Li, W.-J. Zhang, J. Li, H.-Y. Ma, H.-M. Du, D.-C. Li, S.-N. Wang, J.-S. Zhao, J.-M. Dou and L. Xu, *ACS Appl. Mater. Interfaces*, 2020, **12**, 44710–44719.

273 H. Jiang, J. Gu, X. Zheng, M. Liu, X. Qiu, L. Wang, W. Li, Z. Chen, X. Ji and J. Li, *Energy Environ. Sci.*, 2019, **12**, 322–333.
274 S. Chen, L. Zhao, J. Ma, Y. Wang, L. Dai and J. Zhang, *Nano Energy*, 2019, **60**, 536–544.
275 J. Wu, H. Zhou, Q. Li, M. Chen, J. Wan, N. Zhang, L. Xiong, S. Li, B. Y. Xia, G. Feng, M. Liu and L. Huang, *Adv. Energy Mater.*, 2019, **9**, 1900149.
276 B. Chen, X. He, F. Yin, H. Wang, D.-J. Liu, R. Shi, J. Chen and H. Yin, *Adv. Funct. Mater.*, 2017, **27**, 1700795.
277 X. Han, W. Zhang, X. Ma, C. Zhong, N. Zhao, W. Hu and Y. Deng, *Adv. Mater.*, 2019, **31**, 1808281.
278 X. Wang, J. Sunarso, Q. Lu, Z. Zhou, J. Dai, D. Guan, W. Zhou and Z. Shao, *Adv. Energy Mater.*, 2020, **10**, 1903271.
279 X. Zhong, W. Yi, Y. Qu, L. Zhang, H. Bai, Y. Zhu, J. Wan, S. Chen, M. Yang, L. Huang, M. Gu, H. Pan and B. Xu, *Appl. Catal., B*, 2020, **260**, 118188.
280 Q. Xu, H. Jiang, Y. Li, D. Liang, Y. Hu and C. Li, *Appl. Catal., B*, 2019, **256**, 117893.
281 L. An, Z. Zhang, J. Feng, F. Lv, Y. Li, R. Wang, M. Lu, R. B. Gupta, P. Xi and S. Zhang, *J. Am. Chem. Soc.*, 2018, **140**, 17624–17631.
282 X. Wang, Z. Liao, Y. Fu, C. Neumann, A. Turchanin, G. Nam, E. Zschech, J. Cho, J. Zhang and X. Feng, *Energy Storage Mater.*, 2020, **26**, 157–164.
283 X. Yu, Y. Kang, S. Wang, K. S. Hui, K. N. Hui, H. Zhao, J. Li, B. Li, J. Xu, L. Chen and H. Shao, *J. Mater. Chem. A*, 2020, **8**, 16355–16365.
284 W. W. Yin and Z. W. Fu, *ChemCatChem*, 2017, **9**, 1545–1553.
285 H. Yadegari and X. Sun, *Trends Chem.*, 2020, **2**, 241–253.
286 X. Xu, K. S. Hui, D. A. Dinh, K. N. Hui and H. Wang, *Mater. Horiz.*, 2019, **6**, 1306–1335.
287 Q. Sun, J. Liu, B. Xiao, B. Wang, M. Banis, H. Yadegari, K. R. Adair, R. Li and X. Sun, *Adv. Funct. Mater.*, 2019, **29**, 1808332.
288 C. Xia, R. Black, R. Fernandes, B. Adams and L. F. Nazar, *Nat. Chem.*, 2015, **7**, 496–501.
289 J. Y. Cheon, K. Kim, Y. J. Sa, S. H. Sahgong, Y. Hong, J. Woo, S. D. Yim, H. Y. Jeong, Y. Kim and S. H. Joo, *Adv. Energy Mater.*, 2016, **6**, 1501794.
290 Q. Sun, H. Yadegari, M. N. Banis, J. Liu, B. Xiao, X. Li, C. Langford, R. Li and X. Sun, *J. Phys. Chem. C*, 2015, **119**, 13433–13441.
291 H. Yadegari, Y. Li, M. N. Banis, X. Li, B. Wang, Q. Sun, R. Li, T. K. Sham, X. Cui and X. Sun, *Energy Environ. Sci.*, 2014, **7**, 3747–3757.
292 P. Hartmann, C. L. Bender, M. Vračar, A. K. Dürr, A. Garsuch, J. Janek and P. Adelhelm, *Nat. Mater.*, 2013, **12**, 228–232.
293 X. Bi, R. Wang, Y. Yuan, Y. Yuan, D. Zhang, T. Zhang, L. Ma, T. Wu, R. Shahbazian-Yassar, K. Amine, K. Amine and J. Lu, *Nano Lett.*, 2020, **20**, 4681–4686.
294 F. Liang, X. Qiu, Q. Zhang, Y. Kang, A. Koo, K. Hayashi, K. Chen, D. Xue, K. N. Hui, H. Yadegari and X. Sun, *Nano Energy*, 2018, **49**, 574–579.
295 Z. Khan, M. Vagin and X. Crispin, *Adv. Sci.*, 2020, **7**, 1902866.
296 L. Gai, C. Zhao, Y. Zhang, Z. Hu and Q. Shen, *Carbon Energy*, 2022, **4**, 142–154.
297 J. B. Robinson, K. Xi, R. V. Kumar, A. C. Ferrari, H. Au, M.-M. Titirici, A. Parra-Puerto, A. Kucernak, S. D. S. Fitch, N. Garcia-Araez, Z. L. Brown, M. Pasta, L. Furness, A. J. Kibler, D. A. Walsh, L. R. Johnson, C. Holc, G. N. Newton, N. R. Champness, F. Markoulidis, C. Crean, R. C. T. Slade, E. I. Andritsos, Q. Cai, S. Babar, T. Zhang, C. Lekakou, N. Kulkarni, A. J. E. Rettie, R. Jervis, M. Cornish, M. Marinescu, G. Offer, Z. Li, L. Bird, C. P. Grey, M. Chhowalla, D. Di Lecce, R. E. Owen, T. S. Miller, D. J. L. Brett, S. Liatard, D. Ainsworth and P. R. Shearing, *J. Phys. Energy*, 2021, **3**, 031501.
298 J. Tian, F. Xing and Q. Gao, *Molecules*, 2021, **26**, 2507.
299 R. Yan, T. Ma, M. Cheng, X. Tao, Z. Yang, F. Ran, S. Li, B. Yin, C. Cheng and W. Yang, *Adv. Mater.*, 2021, **33**, 2008784.
300 S. Rehman, K. Khan, Y. Zhao and Y. Hou, *J. Mater. Chem. A*, 2017, **5**, 3014–3038.
301 M. R. Kaiser, Z. Han, J. Liang, S. X. Dou and J. Wang, *Energy Storage Mater.*, 2019, **19**, 1–15.
302 Z. Li, Y. Jiang, L. Yuan, Z. Yi, C. Wu, Y. Liu, P. Strasser and Y. Huang, *ACS Nano*, 2014, **8**, 9295–9303.
303 X. Long Huang, S. X. Dou, Z. M. Wang, H.-J. Peng, S. Xue Dou and Z. M. Wang His, *Mater. Horiz.*, 2021, **8**, 2870–2885.
304 F. Pei, L. Lin, D. Ou, Z. Zheng, S. Mo, X. Fang and N. Zheng, *Nat. Commun.*, 2017, **8**, 482.
305 X. Tao, Y. Li, H. guo Wang, X. Lv, Y. Li, D. Xu, Y. Jiang and Y. Meng, *J. Colloid Interface Sci.*, 2020, **565**, 494–502.
306 H. Gao, S. Ning, Y. Zhou, S. Men and X. Kang, *Chem. Eng. J.*, 2021, **408**, 127323.
307 W. Zhou, X. Xiao, M. Cai and L. Yang, *Nano Lett.*, 2014, **14**, 5250–5256.
308 S. Il Choi, M. Shao, N. Lu, A. Ruditskiy, H. C. Peng, J. Park, S. Guerrero, J. Wang, M. J. Kim and Y. Xia, *ACS Nano*, 2014, **8**, 10363–10371.
309 S. Gong, Y. X. Zhang and Z. Niu, *ACS Catal.*, 2020, **10**, 10886–10904.